Walsh, Frank C. and Ponce de Leon, Carlos and Berlouis, Len and Nikiforidis, Georgios and Arenas-Martinez, Luis F. and Hodgson, David and Hall, David (2015) The development of Zn-Ce hybrid redox flow batteries for energy storage and their continuing challenges. ChemPlusChem, 80 (2). 288–311. ISSN 2192-6506 , http://dx.doi.org/10.1002/cplu.201402103

This version is available at http://strathprints.strath.ac.uk/60159/

Strathprints is designed to allow users to access the research output of the University of Strathclyde. Unless otherwise explicitly stated on the manuscript, Copyright © and Moral Rights for the papers on this site are retained by the individual authors and/or other copyright owners. Please check the manuscript for details of any other licences that may have been applied. You may not engage in further distribution of the material for any profitmaking activities or any commercial gain. You may freely distribute both the url (http://strathprints.strath.ac.uk/) and the content of this paper for research or private study, educational, or not-for-profit purposes without prior permission or charge.

Any correspondence concerning this service should be sent to the Strathprints administrator: strathprints@strath.ac.uk

The Strathprints institutional repository (http://strathprints.strath.ac.uk) is a digital archive of University of Strathclyde research outputs. It has been developed to disseminate open access research outputs, expose data about those outputs, and enable the management and persistent access to Strathclyde's intellectual output.

Highlights

- Development and progress in Zn-Ce flow batteries are comprehensively reviewed.
- Electrode thermodynamics, electrode kinetics and cell performance aspects are included.
- The kinetics of Ce redox reactions in sulphuric and methanesulfonic acids are summarised.
- The critical aspects of zinc deposition and stripping in methanesufonic acid are considered.
- The performance of laboratory half-cells and flow cells is illustrated.
- Pilot-scale performance of a flow cell is illustrated and further research is highlighted.

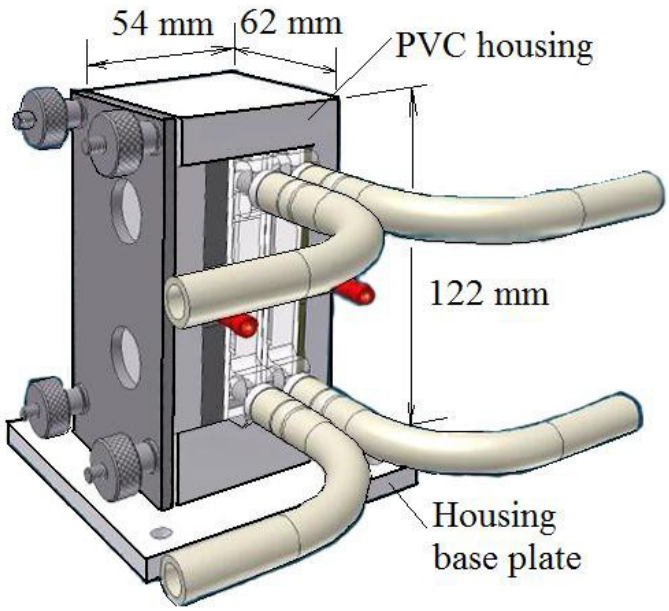
54 mm
62 mm
PVC housing
122 mm
Housing
base plate

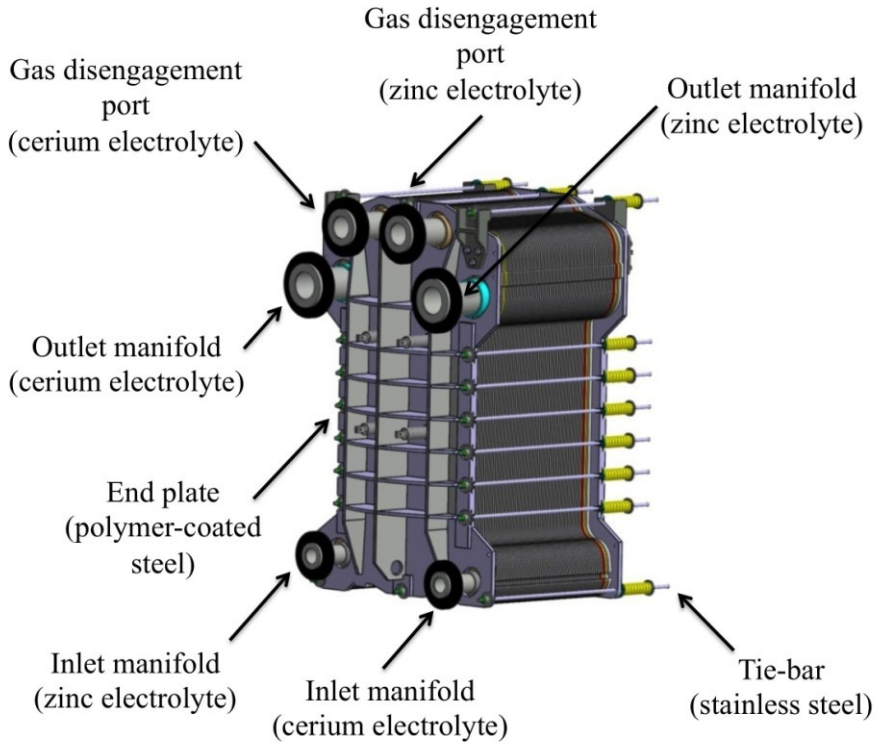
Gas disengagement
port
(cerium electrolyte)
Gas disengagement
port
(zinc electrolyte)
Outlet manifold
(zinc electrolyte)
Outlet manifold
(cerium electrolyte)
End plate
(polymer-coated
steel)
Inlet manifold
(zinc electrolyte)
Inlet manifold
(cerium electrolyte)
Tie-bar
(stainless steel)

Revised version of Invited review paper for ChemPlusChem: Special Issue – Metal-Air and Redox Flow Batteries, 2014. Guest Editors: Jaephil Cho, Linda F. Nazar & Peter G. Bruce
18 August 2014

The development of Zn-Ce hybrid redox flow batteries for energy storage and their continuing challenges

Frank C. Walsh. [a,b] Carlos Ponce de Léon, [a] Len Berlouis, [b] George Nikiforidis, [c] Luis F. Arenas-Martínez, [a] David Hodgson,[d] David Hall. [e]

a. Electrochemical Engineering Laboratory, Engineering Sciences, University of Southampton, Highfield, Southampton, SO17 1BJ, UK

b. WestCHEM, Department of Pure and Applied Chemistry, University of Strathclyde, Glasgow G1 1XL, UK

c. School of Energy and Environment, City University of Hong Kong, Kowloon, Hong Kong.

d. Electrochemical Innovation Lab, Department of Chemical Engineering, University College London, Torrington Place, London WC1E 7JE, UK

e. C-Tech Innovation, Capenhurst, Chester, CH1 6EH, UK

* Author for correspondence; f.c.walsh@soton.ac.uk

Abstract

The Zn-Ce flow battery is a recently introduced hybrid redox flow battery (RFB) but has been extensively studied in the laboratory and at the industrial pilot-scale since its introduction in 2005. The cell has the highest open-circuit cell potentials amongst aqueous RFBs, which can exceed 2.4 V at full charge. While original patents were filed in 2004 and 2005, the history of the half-cell reactions stretches back many decades, the Ce(IV)/Ce(III) redox couple being well studied in sulphuric acid as a redox mediator in organic electrosynthesis or in nitric acid for specialist cleaning in the chemical and nuclear industries while zinc deposition and stripping in acid media are well known in hydrometallurgy and electroplating of metals as well as in other batteries using zinc negative electrodes. Methanesulfonic acid electrolytes were introduced in surface finishing several decades ago but their use in flow batteries is only 20 years old. This review considers the thermodynamics and kinetics of the electrode reactions (desired and secondary) in each half-cell, operational variables, materials for cell components, cell design and performance of the zinc-cerium flow battery. Continuing challenges are highlighted and critical research needs for the science and technological development are considered.

Keywords: Ce(III), Ce(IV), composite electrodes, energy storage, porous, 3-dimensional carbons, Zn(II), zinc deposition.

Contents

1. Introduction
2. The cerium (positive) electrode
2.1 General
2.2 Electrolytes
2.3 Electrochemical measurements
2.3.1 Linear sweep voltammetry
2.3.2 Concentration of methanesulfonic acid
2.3.3 Concentration of cerium (III) methanesulfonate
2.3.4 Electrolyte temperature
2.3.5 Reversibility of the Ce(III)/Ce(IV) redox couple
3. The zinc (negative) electrode
3.1 General
3.2 Common electrode materials
3.3 Porous, 3-D substrates
4. Cell design and performance
4.1 The essential needs of a Zn-Ce cell
4.2 Electrolytes
4.3 Electrodes
4.4 Operational variables
4.4.1 Temperature
4.4.2 Electrolyte flow rate
4.4.3 Current density
4.4.4 Charge conditions and cycle life
5. Scale-up and progression
6. Conclusions and future developments

A review (*ca.* 12,000 words; 18 figures; 7 tables; 108 references)

1. Introduction

Redox flow batteries (RFBs) are one of the most viable technologies for larger scale energy storage and load levelling in grid supply systems and have been the subject of several recent reviews [1-4]. Classical RFBs utilise a solution based redox couple recycled through each half-cell to a reservoir, a common strategy being to separate the half-cells by an ion exchange membrane in a bipolar plate filter-press reactor.

Hybrid RFBs, which combine a solution-based redox couple with an electrode surface/solution electrode reaction (such as solid state transformation, gas evolution/reduction or metal deposition/stripping), include soluble lead, [5] zinc-air, [6] zinc-lead dioxide, [7] zinc-cerium [8] and zinc-bromine [9]. Zinc-air, zinc-bromine and zinc-cerium flow cells have been considered and contrasted in a recent book chapter and the significance of the negative standard potential of the zinc electrode potential has been highlighted [10].

The principle of the Zn-Ce cell is shown in Figure 1. The desired electrochemical reactions are:

At the negative electrode

$$Zn(II) + 2e^- \underset{\text{discharge}}{\overset{\text{charge}}{\rightleftharpoons}} Zn \qquad E^o = -0.76 \text{ V } vs. \text{ SHE} \qquad (1)$$

At the positive electrode

$$Ce(III) - e^- \underset{\text{discharge}}{\overset{\text{charge}}{\rightleftharpoons}} Ce(IV) \qquad E^o = \text{ca. } 1.44 \text{ V } vs. \text{ SHE} \qquad (2)$$

The overall cell reaction is then

$$\overset{\text{charge}}{\rightleftharpoons}$$

$$2Ce(III) + Zn(II) \underset{\text{discharge}}{\overset{\text{charge}}{\rightleftharpoons}} 2Ce(IV) + Zn \quad E_{cell}^{o} = 2.2\ V \qquad (3)$$

The cell reaction corresponds to a thermodynamic energy change, $\Delta G_{cell} = -425$ kJ mol^{-1} Zn. In practice, hydrogen at the negative electrode and oxygen evolution at the positive one can occur as side reactions during charge:

$$2H^{+} + 2e^{-} = H_2 \qquad E^{o} = 0.0\ V\ vs.\ SHE \qquad (4)$$

$$2H_2O - 4e^{-} = 1/2O_2 + 4H^{+} \qquad E^{o} = 1.229\ V\ vs.\ SHE \qquad (5)$$

This water electrolysis results in loss of charge efficiency as well as pH changes near the electrodes and ohmic or safety problems linked with gas evolution. Another loss reaction is the corrosion of the freshly deposited zinc when it is not under sufficient cathodic protection, i.e., the electrode potential is not sufficiently negative (see section 3) and leads to the dissolution of the electrodeposited zinc:

$$Zn + 2H^{+} = Zn^{2+} + H_2 \qquad (6)$$

Some of the main features during the development of the Zn-Ce RFB are indicated in Figure 2. Early work on the Zn-Ce battery was carried out at EDA (which became AIC in 2007), from 1999 in California, USA, and a patent was granted in 2004 [8]. Between 1999 and 2009, EDA/AIC claim to have raised approximately $40 million to support this R&D effort. In 2005, the newly formed company Plurion was opened in Glenrothes in Scotland. In 2009, Scottish Enterprise purchased all of the outstanding shares in Plurion. Later that year, Plurion closed, the

economic downturn being severe for an emerging high technology company with a single product in its early development phase.

The concept of the zinc-cerium battery originally resulted from the high positive standard potential of the Ce(IV)/Ce(III) couple, a high negative potential for Zn dissolution/deposition, the high solubility of metal ions in aqueous methanesulfonic acid [1] and the possibility of generating the highly oxidising, cerium(IV) with good current efficiency at an inert anode [11,12]. In addition, the Ce(IV)/Ce(III)couple has been reported to have relatively fast kinetics in a variety of media [13-19]. The idea to employ methanesulfonic acid as the electrolyte for the zinc/cerium battery was disclosed in US Patents [20, 21] although much of the practical development was carried out later at Plurion [22].

Figure 1 shows this chemistry in a unit cell with a cation exchange membrane and electrolytes containing only zinc(II) and cerium(III). In practice, the battery commonly consists of multiple unit cells compressed together in a bipolar stack with massive end-plates. The size of the electrodes and number of cells determine the maximum battery current and cell potential, respectively. In practice, the membrane is not completely selective to proton transport and over time, mixing of the zinc(II) and cerium(III) ions occurs. This has resulted in operating the battery without a membrane or with both half-cell electrolytes containing both zinc(II) and cerium(III) ions. The performance of each half-cell reaction will be outlined while cell components and cell design will be discussed. In particular, this review considers the importance of operational conditions and cell components on the performance of both divided and undivided cells.

The Zn(II)/Zn couple is attractive as the negative electrode in aqueous redox flow batteries since (a) Zn(II) is highly soluble in many aqueous electrolytes, b) the couple has a more negative standard potential (–0.76 V *vs.* SHE) than almost any other possible couple in aqueous media and c) the reaction has rapid kinetics allowing both charging and discharging with small overpotentials. At this potential, the hydrogen evolution reaction (HER) via proton reduction is thermodynamically the preferred reaction but zinc is a relatively poor electrocatalyst for HER. Hence, charging and discharging a zinc electrode is possible under controlled conditions but performance is always limited by the current efficiency for zinc deposition during charge and the stability of the zinc to corrosion on open-circuit (i.e., during storage in the charged state). The other challenge is to deposit the zinc metal as a compact, uniform layer free of dendrites or voids. With large area electrodes, 'shape change' is a related problem depicted by more pronounced deposition occurring in the lower regions of the cell during charge cycling.

Zinc electrodes have a well-established position in battery technology [1, 10, 23]. Zinc/carbon primary batteries (Leclanché cells) were amongst the earliest batteries while zinc/air and nickel/zinc batteries have also found markets. Amongst all redox flow batteries, the most successful is the zinc/bromine flow battery [24]. The zinc/cerium flow battery continues to attract substantial interest for energy storage, however, primarily due to its relatively large open-circuit cell potential on full charge (E_{cell} = *ca* 2.5 V). The unit Zn-Ce cell is usually operated with acid half-cell electrolytes (usually methanesulfonic acid) with a proton exchange membrane separating the electrodes.

Much of the available information on Zn-Ce flow batteries is due to research at the universities of Southampton and Strathclyde in the PhD programmes of P.K. Leung (2007-2010) [25] and G. Nikiforidis (2008-2011) [26], respectively. In this review, the results of the zinc cerium hybrid

RFB are discussed in terms of the operating conditions of the cell. Charge current densities of 5 mA cm^{-2} to 40 mA cm^{-2} have been employed over the 25-60 ^{o}C temperature range. Several carbon composite materials and porous, 3-D carbon electrodes have been evaluated for use as the negative electrode whilst for the positive electrode, a platinised titanium mesh has typically been employed The half-cells were separated by a Nafion® 117 proton exchange membrane.

2. The cerium (positive) electrode

2.1 General

The Ce(IV)/Ce(III) redox couple has been well studied in sulphuric acid as a redox mediator in organic electrosynthesis [7] or in nitric acid for chemical decontamination and specialist cleaning in the chemical and nuclear industries [27]. The Ce(IV)/Ce(III) redox process, reaction (2), suffers competition from oxygen evolution, reaction (5) during battery charging, which results in a lowering of voltage and charge efficiencies and the need to control current density or potential.

The voltammetry of the Ce(IV)/Ce(III) couple has been studied in a variety of acidic, aqueous solutions and the couple has been found to have quite rapid kinetics [14]. In most media, however, the solubility of the cerium species is insufficient for practical flow battery operation. Interest in Ce(IV) in methanesulfonic acid electrolytes as an oxidising agent in the mediated electrochemical oxidation of organic compounds has generated useful background information for the application of the Ce(IV)/Ce(III)couple in batteries. Preliminary voltammetric studies [28, 29] showed that the Ce(IV)/Ce(III) is a quasi-reversible couple in methanesulfonic acid. Spotnitz et al [30] have reported the solubility of the cerium species as a function of methanesulfonic acid concentration, showing that it declined rapidly above 4 mol dm^{-3} acid. They also reported on its electrolysis in three different parallel plate reactors including a cell

with a reticulated Ti electrode coated with a precious metal oxide catalyst. The performance of the cells declined with anodes in the order PbO_2 > Pt > coated Ti > C. For the Pt electrode, the current efficiency was 96 % at a current density of 100 mA cm^{-2}. Harrison and Theoret [31] extended this development to larger flow cells and investigated the influence of current density, flow rate and anode material. Carbon was not considered a suitable material and the authors employed a DSA-coated titanium. The technology was scaled up for a 100 tonne/year anthraquinone plant where the electrolytic step was the cerium mediated oxidation of naphthalene to naphthaquinone.

Xie et al [32] used cyclic voltammetry to find the appropriate conditions for the use of the Ce(II)/Ce(III) couple in a flow battery. They reported that the Ce(IV)/Ce(III) couple has a more positive standard potential in methanesulfonic acid than in sulphuric acid, consistent with the single charge anion being a weaker complexing agent for Ce(IV). The couple has the advantage that both Ce(IV) and Ce(III) are completely stable up to 60°C although at more elevated temperatures, Ce(IV) may slowly precipitate from electrolytes containing concentrated Ce(IV). The Ce(IV)/Ce(III) couple has rather rapid kinetics at a graphite electrode leading to a cyclic voltammograms with a peak separation close to that expected for a reversible couple. On the other hand, the standard rate constant measured at Pt is significantly lower. At sufficient overpotentials, both the oxidation and reduction reactions may be driven into mass transport control. A parallel plate membrane cell with 3 × 3 cm electrodes was examined as a battery using constant current cycling. The positive electrode here was a 3 mm thick carbon felt with a Ti current collector. One hour charge-discharge cycling at 30 mA cm^{-2} led to a charge efficiency of 86 % and voltage efficiency of 87 %, giving an overall energy efficiency of 75 %.

Leung et al [33] also used voltammetry to examine the kinetics of the couple at Pt and glassy carbon electrodes. Ce(IV) reduction was particularly poor at glassy carbon. Even at Pt, the peak separations were substantial due to the large *IR* drop due to the high Ce(III) concentrations used here in order to mimic the battery situation. As expected, the kinetics became faster at higher temperatures. The optimum concentration of methanesulfonic acid in the electrolyte is a compromise of several factors. A high acid concentration is advantageous to maintain Ce(IV) in solution but this also decreases the solubility of Ce(III). In addition, increasing the concentration of methanesulfonic acid decreased the amount of competing O_2 evolution reaction (OER) during charge but also increased the viscosity of the electrolyte which reduced the mass transfer coefficient. Using a membrane divided cell and a three-dimensional electrode [34], containing either Pt/Ti meshes, graphite felt or carbon felt (to aid the slow kinetics of the Ce(IV)/Ce(III) couple), it was possible to obtain an 80 % conversion of 0.8 mol dm^{-3} Ce(III) to Ce(IV) using a current density of 50 mA cm^{-2} for 4 hours, representing a charge efficiency >75 %.

The use of the Ce(III)/Ce(IV) redox couple has long been suggested as the positive electrode reaction for use in flow batteries [35-37]. This idea was exploited in the zinc-cerium [38-40] and vanadium-cerium redox flow batteries [41] as the couple offers a large positive potential, between 1.28 V and 1.72 V *vs.* SHE depending on the supporting electrolyte [42], and so leads to a high cell voltage for a charged battery.

Cerium in methanesulfonic acid is an attractive half-cell electrolyte for flow battery application as it can be easily prepared at concentrations as high as 1 mol dm^{-3} compared to less than 0.5 mol dm^{-3} in sulphuric acid. In order to optimise the resulting cerium half-cell as the positive electrode reaction in a redox flow battery, an improved understanding of the electrochemical kinetics of the Ce(III)/Ce(IV) redox couple in methanesulfonic acid at different conditions is

crucial. To date, only a limited number of studies have been directed to the electrochemistry of cerium in methanesulfonic acid, the reduction of Ce(IV) and to the reversibility of the Ce(III)/Ce(IV) system. Earlier studies have mainly focused on the oxidation of Ce(III) in sulphuric and nitric acid electrolytes. Previous studies of the oxidation of Ce(III) and reduction of Ce(IV) in methanesulfonic acid have typically used 0.01 to 0.1 mol dm^{-3} cerium (III) methanesulfonate [43-45]. Such a low concentration of the electroactive species is not practical in a redox flow battery since the amount of energy that can be made available in the system depends on the concentration of the electroactive species. These investigations are useful to calculate the kinetic parameters of the Ce(III)/Ce(IV) redox couple but a cerium based flow battery requires a higher concentration of cerium (III) methanesulfonate, typically 0.5 to 2.0 mol dm^{-3} in a wide range of methanesulfonic acid concentration e.g. from 1.0 to 6.0 mol dm^{-3}. This is mainly due to changes in the electrolyte concentration during the charge-discharge cycles. During battery charge, for every Ce(III) oxidised, a proton is transferred to the negative electrolyte from the positive side and the generated Ce(IV) species is complexed by the methanesulfonate anions.

Leung et al have reported the electrochemistry of the Ce(III)/Ce(IV) redox couple in methanesulfonic acid over a range of electrolyte compositions typically found in a redox flow battery [33]. The oxidation of Ce(III) and reduction of Ce(IV) were studied via cyclic voltammetry at a platinum disc electrode and during constant current electrolysis in a divided, two compartment parallel plate flow reactor. The reversibility of the Ce(III)/Ce(IV) redox couple as a function of Ce(III) and methanesulfonic acid concentrations at various electrolyte temperatures was also investigated. The OER was inhibited at high acid concentrations (5 mol dm^{-3}) and this enabled the current efficiency for the interconversion of Ce(III)/Ce(IV) during prolonged constant current batch electrolysis to be maintained at ~95%.

2.2 Electrolytes

Figure 3 shows the cyclic voltammetry of the Ce(III)/Ce(IV) redox couple recorded at platinum and glassy carbon disk electrodes in an electrolyte containing 0.8 mol dm^{-3} cerium(III) methanesulfonate and 4.0 mol dm^{-3} methanesulfonic acid at 22 ^{o}C using a potential sweep rate of 50 mV s^{-1}. The oxidation of Ce(III) started at approximately + 1.2 V *vs.* Ag|AgCl on both electrodes and the anodic current rose steadily as the potential became more positive. A higher current density of 39 mA cm^{-2} was recorded on the platinum electrode compared with *c.a.* 25 mA cm^{-2} on the glassy carbon electrode at around 1.65 V *vs.* Ag|AgCl for both electrodes. At a more positive potential, the anodic current at the glassy carbon electrode decayed while at the platinum electrode continued to rise sharply due to the oxygen evolution reaction (and the formation of platinum oxides) [46,47]. The influence of oxygen evolution reaction does not seem to be significant on the glassy carbon electrode as the current during the oxidation of Ce(III) on this electrode did not increase at more positive potentials. However, this can also be attributed to the oxidation of carbon at such potential. On the reverse scan, a more negative potential was required for the reduction of Ce(IV) on the glassy carbon than on the platinum electrode. A maximum cathodic peak current density of 15 mA cm^{-2} on platinum was observed at *c.a.* + 1.05 V *vs.* Ag|AgCl while only 7.5 mA cm^{-2} at + 0.65 V *vs.* Ag|AgCl at the glassy carbon electrode. The separation between the oxidation and reduction peaks on each electrode was approximately 0.7 V on platinum and 1.0 V on carbon. The anodic current was higher than the cathodic one and the ratio of cathodic to anodic peak current was approximately 0.4 to 0.6 on both electrodes. Platinum gives a more favourable electrochemical response than carbon for the oxidation of Ce(III) and reduction of Ce(IV) in methanesulfonic acid because the peak separation is smaller. Several features in the voltammogram are worth mentioning: the separation of peak potentials is relatively high (several hundreds of millivolts) and the ratio of

cathodic to anodic peak current is far below 1, the value expected for an ideally reversible system. The magnitude of oxygen evolution as a secondary reaction on the platinum electrode also needs to be reduced in order to improve the current and conversion efficiencies. Since platinum gave a higher oxidation current than glassy carbon and the separation between the oxidation and reduction peaks was smaller than using the glassy carbon electrode in the cyclic voltammograms, subsequent studies were carried out on a platinum electrode.

2.3 Electrochemical measurements

2.3.1 Linear sweep voltammetry

Figure 4a) shows the effect of the potential sweep rate on the cyclic voltammetry of the Ce(III)/Ce(IV) redox couple on a platinum electrode in an electrolyte containing 0.8 mol dm^{-3} cerium (III) methanesulfonate and 4.0 mol dm^{-3} methanesulfonic acid at 22 ^{o}C. The peak current density of the oxidation and reduction processes increased linearly with the square root of the potential sweep rate. Figure 4b) shows the linear Randles-Sevćik relationship [48-50] indicating that the oxidation of Ce(III) and reduction of Ce(IV) in methanesulfonic acid were diffusion limited. In this work, the diffusion coefficient (D) of cerium(III) ion was determined using the anodic current densities as the experiment was carried out in the cerium(III) electrolyte. Using the value of the slope from this plot during the oxidation process, the diffusion coefficient of Ce(III) ion in methanesulfonic acid was estimated to be 1.67×10^{-6} cm^2 s^{-1} at 22 ^{o}C. This value agrees with previous measurements of diffusion coefficients that where in the range of 0.27 to 0.72×10^{-6} cm^2 s^{-1} [51], using a glassy carbon electrode in an electrolyte containing 0.034 to 0.152 mol dm^{-3} cerium (III) methanesulfonic in 1.0 and 4.0 mol dm^{-3} methanesulfonic acid at room temperature.

The *D* value of Ce(III) ions in methanesulfonic acid was slightly smaller than those reported for many metal ions in aqueous electrolytes, which are typically (4.0 to 6.0) × 10^{-6} cm^2 s^{-1} [52,53] possibly due to the complexation with the methanesulfonate anions [45]. Indeed, lower diffusion coefficient values were found at increased methanesulfonic acid concentration, e.g. in an electrolyte containing 0.152 mol dm^{-3} cerium (III) methanesulfonate, the diffusion coefficient of Ce(III) was approximately 0.69 × 10^{-6} cm^2 s^{-1} in 1.0 mol dm^{-3} methanesulfonic acid but only 0.27 × 10^{-6} cm^2 s^{-1} in 4.0 mol dm^{-3} methanesulfonic acid [51].

At all potential sweep rates, the ratio of cathodic to anodic peak current was approximately 0.5. The charge density for the reduction of Ce(IV) was lower than that involved in the oxidation of the Ce(III) ion possibly due to the OER secondary reaction. Earlier investigations also suggested that the larger anodic peak current could also be due to the contribution of the weak adsorption of Ce(III) ions on the electrode surface, which was demonstrated via cyclic voltammograms of the Ce(III)/Ce(IV) redox couple in sulphuric and methanesulfonic acids [45]. Recent studies have also shown that the cathodic and anodic peak currents can be brought closer via the complexation of Ce(III) and Ce(IV) ions with ligands such as ethylenediaminetetraacetic acid and diethylenetriaminepentaacetic acid [54,55]. Such a strategy has been advantageous since the reversibility of the Ce(III)/Ce(IV) redox couple was significantly improved and higher charge densities were obtained [56]. The work also showed that the faster electrochemical kinetics in the presence of the ligands are due to a higher charge transfer coefficient and an increased electron transfer rate constant for the Ce(III) ⇆ Ce(IV) redox reaction. The electron transfer rates were also found to be similar for the oxidation of Ce(III) and the reduction of Ce(IV), confirming that an improvement in the reversibility of these reactions could be achieved using complexing ligands [56].

By increasing the potential sweep rate during the oxidation of Ce(III), the peak potential shifted to more positive values while for the reduction of Ce(IV) to more negative potentials. The separation of the peak potentials increased at higher potential sweep rates e.g. 560 mV at 8 mV s^{-1} compared to 790 mV at 64 mV s^{-1}. Devadoss, Noel, Jayaraman and Basha [43] reported in an electrolyte containing 0.034 mol dm^{-3} cerium (III) methanesulfonate in 4.0 mol dm^{-3} methanesulfonic acid at a glassy carbon electrode that the reduction peak shifted by approximately –100 mV as the potential sweep rate increased from 10 to 160 mV s^{-1}. Earlier investigations also showed a quasi-reversible behaviour of the Ce(III)/Ce(IV) redox couple in commodity electrolytes, such as sulphuric acid [35, 57]. These observations suggest poor reversibility of the Ce(III) to Ce(IV) reaction.

2.3.2 Concentration of methanesulfonic acid

Cyclic voltammograms of the Ce(III)/Ce(IV) redox couple were recorded at a platinum electrode in a wide range of methanesulfonic acid concentration from 0.1 to 5.0 mol dm^{-3}. Figure 5a) shows that the anodic current density for the oxidation of Ce(III) decreases as the concentration of methanesulfonic acid increased when the electrolyte contained 0.8 mol dm^{-3} Ce(III) methanesulfonate. For example, the anodic peak current density was approximately 50 mA cm^{-2} in 2.0 mol dm^{-3} methanesulfonic acid but no oxidation peak (but a plateau) was observed with 5.0 mol dm^{-3} acid concentration, although the current density reached 20 mA cm^{-2}. The change in the peak current density was due to the increase in the solution viscosity at high acid concentrations and to the high conductivity of the acid at low concentrations in aqueous electrolytes [33]. Other findings reported in the literature also showed similar observations: the anodic peak current was 3.6 mA cm^{-2} in 1.0 mol dm^{-3} methanesulfonic acid and decreased to 1.6 mA cm^{-2} in 6.0 mol dm^{-3} methanesulfonic acid in a solution where the starting electroactive species was Ce(IV) at 0.033 mol dm^{-3} concentration [45]. A further increase in the anodic

current after the oxidation of Ce(III) was caused by oxygen evolution, which was found to be influenced by the methanesulfonic acid concentration. The linear sweep voltammograms in the absence of Ce(III) with different concentrations of the acid in Figure 5b) show that oxygen evolution shifted to more positive potentials at a higher acid concentration. For example, at an electrode potential of *c.a.* +1.8 V *vs.* Ag|AgCl, the anodic current density was *c.a.* 80 mA cm^{-2} in 2.0 mol dm^{-3} methanesulfonic acid, but at the same potential the current density was only 40 mA cm^{-2} in 5.0 mol dm^{-3} methanesulfonic acid. Although similar behaviour has been found in sulphuric acid [58], the cathodic current density was smaller. These findings suggest that the oxidation of Ce(III) is the dominant reaction at higher concentrations of methanesulfonic acid and is consistent with observations during the experiment where less oxygen bubbles appeared on the electrode surface during the oxidation of Ce(III) under these conditions.

Figure 5c) shows the charge density involved in the oxidation and reduction of Ce(III) and Ce(IV) ions respectively, *vs.* the concentration of methanesulfonic acid. The charge density calculated from the area under the curve of the cyclic voltammogram, during the oxidation of Ce(III) is constant up to 1 mol dm^{-3} of methanesulfonic acid and then decreases sharply as the acid concentration increases. This is consistent with the observations made on the cyclic voltammograms shown in Figures 5a) and 5b). The charge density for the reduction of Ce(IV) increased significantly with the concentration of acid up to 1 mol dm^{-3}, after that the charge increase is slow and reaches a maximum at 4.0 mol dm^{-3} methanesulfonic acid. A further increase in the acid concentration led to a slight reduction in both charge and current density for the reduction of Ce(IV). This is attributed to an increase in solution viscosity [59] and the solubility limit of Ce(III) in 5.0 mol dm^{-3} in methanesulfonic acid, which might have been exceeded. At such a high acid concentration, the solubility limit of Ce(III) was estimated to be approximately 0.7 mol dm^{-3} [44].

2.3.3 Concentration of cerium (III) methanesulfonate

Figure 6 shows that the charge density for both the oxidation of Ce(III) and reduction of Ce(IV) increased when the Ce(III) methanesulfonate changed from 0.1 to 1.0 mol dm^{-3} in a solution containing 4.0 mol dm^{-3} methanesulfonic acid. A further increase in the concentration of cerium (III) methanesulfonate to 1.2 mol dm^{-3}, which was a relatively viscous solution, led to a reduction in the charge density for both processes. This was due to the limited solubility of Ce(III) at such acid concentration as previous results showed that 1.0 mol dm^{-3} was the solubility limit for Ce(III) and Ce(IV) in 4.0 mol dm^{-3} methanesulfonic acid at room temperature [44, 60]. This observation is also consistent with previous results where a high concentration of Ce(III) could only be achieved in a low concentration of methanesulfonic acid. The concentration of Ce(IV) however, could only be increased in higher methanesulfonic acid concentrations [44].

Since the acidity of the electrolyte in the flow battery will change during charge-discharge cycles, the challenge is to use an appropriate concentration of methanesulfonic acid which provides sufficient solubility for both Ce(III) and Ce(IV) species. The above results indicate that a solution with higher concentration of Ce(III), e.g. 1.5 to 2.0 mol dm^{-3} could be prepared in a low acid concentration. However, the Ce(IV) solution obtained during or from a constant current electrolysis under these conditions was highly viscous with evidence of a slurry [60]. A high concentration of Ce(IV) could be prepared if the concentration of the acid was high but the solubility of Ce(III) became limited and the Ce(III)/Ce(IV) redox couple demonstrated poor reversibility. Therefore, a solution of 0.8 mol dm^{-3} cerium (III) methanesulfonate was prepared in 4.0 mol dm^{-3} methanesulfonic acid as a compromise in order to maximize the solubility of both Ce(III) and Ce(IV) ions for the system.

2.3.4 Electrolyte temperature

Figure 7 shows that the charge density during the oxidation of Ce(III) increases with temperature. The reduction of Ce(IV) also increased but reached a maximum at 50 ^{o}C. The higher charge density for the oxidation of Ce(III) could be due to the simultaneous oxygen evolution reaction which is favourable at high temperatures. Cyclic voltammograms recorded for 0.01 mol dm^{-3} Ce(III) in 1.0 mol dm^{-3} sulphuric acid also showed an increase in the charge density at elevated electrolyte temperature, e.g. 60 ^{o}C [35]. During the electrolysis of Ce(III) ions in both undivided

and divided electrochemical cells in 3.0 mol dm^{-3} nitric acid electrolyte, the applied cell potential difference decreased slightly as the temperature increased due to improved reaction kinetics, increased electrolyte conductivity and reduced viscosity. The study also showed that the current efficiency of the electrolysis of Ce(III) to Ce(IV) improved from 77 % at 40 ^{o}C to 93 % at 90 ^{o}C in nitric acid [59].

An increase in the diffusion coefficient of Ce(III) ions and the rate constant for Ce(III) oxidation have also been observed at elevated electrolyte temperature [42]. Literature studies confirmed that an Arrhenius, semi-logarithmic plot of the diffusion coefficient against the inverse of the electrolyte temperature is a linear relationship for the Ce(III) ⇆ Ce(IV) redox reaction in nitric and sulphuric acid electrolytes [58].

2.3.5 Reversibility of the Ce(III)/Ce(IV) redox couple

Cyclic voltammetry studies at a platinum electrode in various electrolyte compositions have been used to assess the reversibility of the Ce(III)/Ce(IV) redox couple, *viz.*, in terms of the

separation of the anodic and cathodic peak potentials and the ratio of cathodic to anodic peak currents. Tables 1A and 1B summarise the results of cyclic voltammetry studies in sulphuric acid and in other electrolytes for the proposed Zn-Ce RFBs. Table 2 shows data relating to the reversibility of the Ce(IV)/Ce(III) system under different conditions. The peak separation of potentials decreased at lower concentrations of cerium (III) and methanesulfonic acid as well as at higher electrolyte temperatures. The ratio of cathodic to anodic peak current density varied from 0.3 to 0.65 depending on the electrolyte composition. The ratio was closer to unity in an electrolyte containing a higher concentration of methanesulfonic acid and cerium (III) methanesulfonate as well as at an elevated electrolyte temperature (50 °C).

At higher concentrations of cerium (III) methanesulfonate and methanesulfonic acid, the separation of oxidation and reduction peak potentials increased due to an increase in the ohmic drop associated with larger current response and changes in the solution viscosity and conductivity. The high concentration also reduced the reversibility of the Ce(III)/Ce(IV) redox couple. At such concentration, the oxidation potential remained fairly constant but the reduction potential became more negative leading to lower discharge cell potential difference of a cerium-based redox flow battery. These observations agree with other studies, for example the separation of peak potentials increased from 140 mV to 240 mV when the acid concentration changed from 2 to 5 mol dm^{-3} in a solution containing 0.033 mol dm^{-3} of Ce(III) [45].

Although a low concentration of cerium (III) methanesulfonate leads to a narrower separation of the peak potentials, such a low concentration of Ce(III) ions would not be practical for flow battery applications. Besides, the use of a low concentration of methanesulfonic acid also limits the solubility of Ce(IV) in the solution, hence the energy density available in a flow battery will be limited. A solution of 0.8 mol dm^{-3} cerium (III) methanesulfonate in 4.0 mol dm^{-3}

methanesulfonic acid has been suggested for flow battery applications. The use of elevated electrolyte temperature could also provide a more reversible redox reaction but the temperature range will be limited by the properties of the electrode materials as well as those of the electrolytes. Table 2 summarises the impact of typical operational conditions used in RFBs on the reversibility of the Ce(III)/(IV) redox couple.

3. The zinc (negative) electrode

3.1 General

As in all hybrid zinc redox flow battery systems [1-3], zinc is deposited on an inert collector during charge. The zinc-halogen hybrids are amongst the most studied of the Zn-based redox flow battery systems. Factors found to affect the zinc deposition include the electrode substrate, the charging method, the cell geometry, the electrolyte hydrodynamics, the electrolyte composition and the zinc electrode morphology. An investigation of zinc electrodeposition in sulphuric acid has been carried out by Guillaume et al [61] who reported that the HER on stainless steel was inhibited by the zinc deposits and that the deposit morphology was not significantly influenced by current density. They also reported that increasing the concentration of the zinc species (>2 mol dm^{-3}) would yield higher deposition current efficiencies of 80%. However, some of the problems with the zinc-bromine battery does involve the HER at the negative electrode on charge, which leads to lower charge efficiencies and also to non-uniform deposition of zinc on random cycling [1]. Van Parys et al [13] investigated the zinc deposition mechanism with simultaneous hydrogen evolution in an acidic sulphate solution (5×10^{-2} mol dm^{-3} $ZnSO_4$ in 1 mol dm^{-3} Na_2SO_4). It was found that if gas bubbles were formed in the mass transport controlled region, the induced micro stirring increased the current density whereas if the current was kinetically controlled, the current density decreased due to the increased resistance of the electrolyte [13]. In the zinc-nickel cell, zinc dendrite penetration of the

separator and redistribution of the zinc electrode active material on cycling as well as de-zincification of the zinc electrode were found to be occur [13]. For this system, Ito et al [16] reported that high electrolyte flow velocities, i.e. >15 cm s^{-1}, improved the cycle life of the battery at 100 % depth of discharge.

In the industrial electrodeposition of metals, electrolyte additives are routinely used to control the morphology and appearance of the deposits. Another objective of such additives is to reduce simultaneous hydrogen evolved during the metal deposition process, *viz.* during the charging of the battery. Classical glue and gum Arabic are the most commonly used additives in the industry for the zinc electrowinning process [17, 18]. Glue has been reported to decrease the grain size of the zinc deposit while gum Arabic changes the deposits orientation (basal to the intermediate

plane). The search for better organic additives is still ongoing. It has been reported [18] that TBABr (tetrabutyl ammonium bromide) can act as a dendritic growth suppressor whilst also increasing the compactness of zinc deposits in alkaline zincate electrolytes. Increasing the additive concentration though can also lead to the blockage of the active nucleation sites on the cathode surface by adsorption of the additive, thereby decreasing the overall energy efficiency. The use of gelatin (solid content: 80 mL g^{-1}) to chlorine based electrolytes (pH = 4) has been shown to decrease the adsorption of H^+ ions on active zinc sites and increasing the energy efficiency at 40 °C [20].

Two synthetic organic additives with superior performance to glue and gum Arabic have been identified as nonylphenoloxylethylene [22] and 2-butyne-1, 4-diol [23]. The latter has been reported to improve the zinc current efficiency in the presence of Ni impurities in an acidic sulphate solution. Furfuraldehydethiosemicarbazone (FrTSCN) and salcylaldehyde

thiosemicarbazone (SaTSCN) have also been reported to achieve current efficiencies as high as 99 % and 97 %, respectively for zinc deposition in both alkaline and acidic solutions [62]. Ichino et al [63] found that Pb(II) ions can be adsorbed at the electrode surface and strongly inhibit the HER reaction during the zinc deposition process from acidic sulphate electrolytes. Both thiourea and urea are known to improve the crystallographic orientation of the zinc deposits at pH = 0.5 [64]. In addition, it has been reported that decreasing the pH from 5.4 to 1 of a zinc electrolyte, containing chromium in 0.6 mol dm^{-3} $ZnSO_4.7H_2O$ still allowed zinc deposition to occur well before the HER process [65]. The reduction in the pH resulted in a fall in the formation of hydroxo-products of chromium in the electrolyte. Furthermore, compounds like indium have been reported to increase the hydrogen overpotential [66]. The same effect has been reported for polyethylene glycols (PEGs). [67]**.** It is important though that future studies should move in the environmental direction by investigating sustainable inhibitors and use of natural product extracts.

3.2 Common electrode materials

Carbon-based composites are the most widely employed materials for the negative electrode in the Zn-Ce hybrid RFB system [34, 68-71]. Much development has taken place over the last 20 years on these composite materials and various forms have been studied. Pure carbon and graphite tend to be brittle and often difficult to work with. Hence, scaling-up to large dimensions for use in stacks becomes a significant issue. As a result, composites of polymer binders and conductive particles, such as carbon polymer composites [72, 73] and polymer-impregnated graphite plates [34, 70, 74] are often used. These have the advantages of being low cost, light in weight and having improved mechanical properties. A list of the carbon substrates is presented in Table 3 with details of their physical properties and manufacturer. Electrodes based on

expandable graphite have low through-plane electrical resistivity as well as low thermal expansion but chemical stability in the methanesulfonic acid electrolyte used in the Zn-Ce system is quite poor. On the other hand, the carbon composite materials, which are held together by polymer binders, such as polyvinylidene difluoride, PVDF and high density polyethylene, HDPE, [75] phenolic resin [75, 76] and polyvinyl ester (PVE) [77] have been found to be chemically robust. These composites are commonly manufactured by compression/injection moulding.

Cyclic voltammetry (Figure 8) has been carried out on these electrodes in neutral solutions of sodium methanesulfonate containing 0.01 – 0.1 mol dm^{-3} Zn^{2+} ions (Figure 8a) as well as in more concentrated zinc solutions (0.7 mol dm^{-3} to 2.0 mol dm^{-3}) in methanesulfonic acid, (Figure 8b) [25,26,33,34,70]. A clear decrease in the potential for zinc nucleation with temperature can be seen from Table 4, *e.g.* from –1.60 V *vs.* $Hg|Hg_2SO_4|$sat'd K_2SO_4 at 25 °C to –1.54 V *vs.* $Hg|Hg_2SO_4|$sat'd K_2SO_4 at 60 °C for the carbon-PVDF composite electrode [70].

Rotating disk electrode (RDE) studies in this electrolyte allowed the diffusion coefficient of the zinc(II) species to be obtained at different temperatures [25,26,33,34,70]. The value of D increases with temperature from 4.8×10^{-6} cm^2 s^{-1} at 25 °C to 8.5×10^{-6} cm s^{-1} at 40 °C and 12.7×10^{-6} cm^2 s^{-1} at 60 °C, associated with a decrease in the viscosity of the electrolyte, from 0.0136 Pa s at 25 °C to 0.0056 Pa s at 60 °C. Further studies using the RDE system have been carried out in order to obtain the standard heterogeneous electron transfer rate constant, $k°$ for the reaction at these composite electrodes [26, 70]. Data are taken from the mixed controlled region of the RDE j-E curve using the Koutecky-Levich equation to determine the kinetic parameters at potentials within this region (Figure 9). The $k°$ value is then obtained from the plot of ln k *vs.* E according to:

$$lnk = lnk^{o} - \frac{\alpha nFE}{RT} \qquad (8)$$

when $E = E_{½}$, the half-wave potential chosen at the lowest rotation speed. The calculated rate constant showed substantial variations for the various carbon-polymer composites substrates.

The HDPE-2 carbon composite exhibited slightly faster kinetics ($k°$ = 1.57 × 10^{-3} cm s^{-1} at 25 °C) compared to the other electrodes. For the C-PVDF, glassy carbon and HDPE-2 carbon composite substrates, the rate constant increased from 1.16 × 10^{-3} cm s^{-1} to 2.32 × 10^{-3} cm s^{-1} when the temperature was increased from 40 °C to 60 °C. The standard rate constant of the PVE electrode was smaller by a factor of 3.5 compared to the one of the HDPE-2 carbon, indicating that kinetics on this electrode surface are slow, even at 60 °C. Interestingly, the values of Mendoza et al [78] in chloride solution (0.5 mol dm^{-3} $ZnCl_2$ and 0.4 mol dm^{-3} H_3BO_3) for the standard rate constant was 8.73 × 10^{-3} cm s^{-1} for the glassy carbon electrode compared to 1.60 × 10^{-3} cm s^{-1} in the methanesulfonate medium, emphasising the important role played by the $CH_3SO_3^-$ counter ions in adsorption and complexation of the depositing species.

The nucleation and growth of zinc at the negative electrode on charge has been examined by current density *vs*. time behaviour (Figure 10). The potential at which zinc deposition begins is seen to decrease at higher temperatures but some variation occurs on the different carbon-polymer composite surfaces, as indicated in Table 4. Nucleation studies on various carbon electrode surfaces have been carried out in solutions containing different concentrations of zinc(II) in 5.7 mol dm^{-3} MSA, using potential steps in the range from –1.60 V to –1.85 V *vs.* $Hg|Hg_2SO_4$ at 60 °C [70]. The data were analysed using the approach developed by Scharifker

and Hills [79] for instantaneous and progressive nucleation and growth of the nuclei. Normalised plots for the nucleation of zinc at –1.68 V *vs.* $Hg|Hg_2SO_4$ on the PPG86 composite carbon electrode presented in Figure 10a indicates that the nucleation here (and indeed on the other composite materials) occurred via the instantaneous route [70]. The nucleation densities on various carbon composite electrodes in 0.7 or 1.5 mol dm^{-3} Zn(II) + 5.7 mol dm^{-3} methanesulfonic acid are given in Table 5. The data from these tables clearly show N_o increasing at more negative potentials and depending on the electroactive species concentration. The N_o values found for the solution containing 0.01 mol dm^{-3} Zn(II) are in a similar range to the ones found by Marquez et al [80] for silver nucleation on glassy carbon electrodes from silver cyanide solutions and by Yu et al [81] for zinc nucleation on glassy carbon from sulphate, chloride and acetate solutions at 25 °C.

With an increase in temperature to 60 °C, the deposition potentials are considerably higher for the PVE and PVDF electrodes, albeit at a lower zinc composition, Figure 10b) [26, 70]. For the PVE carbon composite electrode, the difference was 310 mV while for the PVDF composite it was *ca.* 140 mV. This unusual behaviour may be linked to the nature of the composite electrode material. The higher temperature could lead to the expansion of the matrix which in turn would reduce the electrode conductivity and so necessitating the need for the higher potential observed. Yu et al., [81] showed that elevated temperatures resulted in increased N_o values in an alkaline Zn/MnO_2 battery but this study however used glassy carbon electrodes. Similar analyses have been conducted for deposition from higher zinc concentrations (0.7 mol dm^{-3} and 1.5 mol dm^{-3}) in 2.4 mol dm^{-3} MSA except that deviations in the experimental curves occur at longer times, possibly due to changing surface area of the deposit and some contribution from hydrogen evolution.

The behaviour of these electrodes under multiple galvanostatic charge-discharge cycles has also been examined [26, 70]. The parameters varied here were the current densities employed, the duration of the charge, the temperature and the flow velocity. Typical chronopotentiometry data recorded during these experiments are shown in Figure 11 which shows a steady potential of *ca.* –1.68 V *vs.* $Hg|Hg_2SO_4$ during zinc deposition and *ca.* –1.2 V *vs.* $Hg|Hg_2SO_4$ during dissolution at a current density of 50 mA cm^{-2} at 60 °C. The open-circuit potential of –1.41 V *vs.* $Hg|Hg_2SO_4$ is consistent with zinc electrodeposition on the composite carbon surface and the data indicates that the overpotentials for the deposition and dissolution processes are similar in magnitude. The charge efficiencies (η_C) evaluated from these curves for several of the composite electrodes are shown in Figure 12. The results indicate that the C-PVDF and the HDPE-1 composite materials gave the best performance of all the electrodes examined here with η_C averaging 96 %. The PVE and HDPE-2 electrodes exhibited η_C values averaging 95 % and 93 %, respectively. The glassy carbon electrode data is included in the figure to illustrate the superior behaviour of the carbon-polymer composites, especially the C-HDPE, C-PVDF and C-PVE materials, in achieving high charge efficiency for the zinc half-cell reaction of the hybrid Zn-Ce system.

The effect of charging time on the charge efficiency and on the stability of the zinc electrodeposits was also examined in a study where the composite material was mounted onto a rotating disk set up and this also allowed the impact of solution velocity to be evaluated [26,70]. As the data of Figure 13 indicates, an electrode rotation rate of 10 Hz (*Re* = 200) for the C-PVDF electrode, stable deposits (capable of remaining on the material surface then undergoing anodic dissolution) could be formed over the charging duration of 5 min or less. At that current density (50 mA cm^{-2}), longer charging periods appeared to give rise to less uniform deposits which could become dislodged from the electrode substrate.

Zinc-based systems tend to suffer from a high rate of self-discharge because of the highly reducing zinc species. The main problem here is the high corrosion rate of the zinc electrodeposit in the acid electrolyte via hydrogen evolution. Thus, the discharge current density is important in this Zn-Ce system, since the freshly electrodeposited zinc is sitting in an electrolyte consisting of ca. 2 mol dm^{-3} H^{+}. Indeed, as Figure 14 shows, discharge current densities below 50 mA cm^{-2} lead to a substantial loss in the charge efficiency and this is mostly attributed to open-circuit corrosion of the zinc. The corrosion rate of zinc deposits has been measured under different conditions by Tafel extrapolation, weight loss and hydrogen evolution measurements giving the values shown in Table 6 [82]. The zinc corrosion is enhanced by high acid concentrations and elevated temperatures but decreased at higher Zn(II) ion concentration. Considering this aspect and the accompanying higher current efficiency during charging and high charge capacity, a high zinc ion concentration is desirable.

Corrosion inhibitors such as cetyltrimethylammonium bromide (CTAB) and butyltriphenyl phosphonium chloride have been successfully tested in these solutions, achieving 40% inhibitive efficiency in 1 mol dm^{-3} MSA over a 10 h period [25,82]. Lead(II) ions were also found to be very effective (ca. 90 %) over a 4 h duration but this decreased to less than 7 % over the 10 h period. These compounds, along with TBAOH, potassium sodium tartrate and indium oxide have also been employed as additives to control the morphologies of the zinc deposits with varied degree of success. However, the microstructure of the electrodeposits, even without these additives, was quite smooth with little evidence of dendritic growth, due to the presence of methanesulfonate ions. [25, 68]

4. Cell design and performance

4.1 The essential needs of a Zn-Ce cell

The essential components of a traditional unit Zn-Ce flow cell are a positive and negative electrode experiencing a controlled reaction environment and divided by a proton exchange membrane. The usual choice of cell stack is the parallel plate reactor in the bipolar electrode, filter-press mode [83, 84].

In work carried out at the University of Southampton, Leung et al described the operation of a divided laboratory cell (Figure 15) [25,34] consisting of two acrylic chambers provided with flow channels and separated by a Nafion® 115 proton membrane. A PVC casing was used to hold and press the cell components. The positive and negative electrodes were placed in their corresponding half-cells with a membrane-electrode gap of 11 mm. Each electrode had an active surface area of 9 cm^2. In order to avoid leaks, silicone rubber gaskets were placed between the cell components to provide an elastomeric seal. Planar carbon-polyvinyl ester composite was used as the negative electrode and several 2-D and 3-D materials were tested as the positive electrode. It was found that platinized titanium mesh and carbon felt yielded the best performance, while the 2-D materials gave poor results. Low current densities at the positive electrode were beneficial for the cerium reaction. Under optimal conditions, the cell showed a charge efficiency of 99.4 % and an energy efficiency of 59.3 %. The different composition of the electrolytes used in each side of the membrane promoted the migration of protons into the negative half-cell. The resulting change of acidity was the main issue affecting the capability of the cell, especially in the positive compartment.

Nikiforidis et al at the University of Strathclyde used a divided Zn-Ce laboratory flow cell to test the performance of polyvinyl ester and polyvinylidene fluoride-carbon composite materials as

negative electrodes, as well as the operational conditions of the system [26, 85]. A platinized titanium mesh was used as positive electrode. The anode and cathode compartments were separated by a Nafion® 117 membrane. Both electrodes had a geometric area of 100 cm^2, which makes them the largest electrodes evaluated outside of Plurion. Each half-cell had custom-designed channels to ensure a uniform flow of the electrolytes, which were recirculated with a peristaltic pump. Silicone rubber gaskets were used to adjust the separation of the cell components. This cell yielded charge efficiencies of more than 90 % and energy efficiencies above 60 % at 10 mA cm^{-2}, values similar to those obtained by Leung et al. [34] The electrodes tested with this cell were cycled over 100 times with good stability, indicating that this system is suitable for the pilot-scale.

An undivided cell (Figure 16) has also been described by the group at the University of Southampton [69]. Both electrodes were placed in a single chamber of the cell, eliminating the need for a membrane as only one electrolyte was needed for the cell operation. The positive electrode consisted of carbon felt compressed onto a planar carbon polyvinyl ester, while planar carbon polyvinyl was used as the negative electrode. The exposed surface of each electrode was 1.6 cm^2, with a separation of 2 cm. As well as avoiding the cost of the membrane and the ohmic drop associated with it, the use of a single methanesulfonic acid electrolyte, containing cerium and zinc ions, greatly simplifies the flow system associated with the cell. The use of carbon felt gave low overpotentials at the positive electrode but the carbon felt eventually suffered from oxidation. The cell could be operated over a range of current densities (20-80 mA cm^{-2}) and the improved voltage efficiency, expected in the absence of membrane, was achieved. At 20 mA cm^{-2}, the battery could be cycled and the charge and energy efficiencies were 82 % and 72 %, respectively. Of course, the presence of Ce(IV) in the electrolyte in the charged state led to a further increase in the rate of zinc corrosion and self-discharge was complete in a few hours. A

possibility might be to operate the cell with a reduced area of negative electrode.

The usual industrial design for a redox flow battery system is the bipolar filter-press stack with internal electrolyte manifolds which is discussed in section 5. Such a cell may accommodate different electrode surfaces for the positive and negative electrodes, which may be coated or uncoated 3-D materials or planar carbon-polymer composites.

4.2 Electrolytes

The concentration of the redox species in a RFB is directly related to the current output of the battery. In the Zn-Ce system, the concentration of the acid also determines the solubility of the cerium species and even the overall durability of the device. Thanks to its capacity to dissolve cerium ions in relatively high concentrations, MSA has been used as support electrolyte in most reported Zn-Ce cells. [30]

Divided cells use two different electrolytes, one for each half-cell. Leung et al used 0.8 mol dm^{-3} Ce(III) dissolved in 4.0 mol dm^{-3} MSA for the positive half-cell and 1.5 mol dm^{-3} Zn(II) in 1.0 mol dm^{-3} MSA for the negative half-cell. [33, 34]. The difference in the composition of the electrolyte allowed ions to migrate through the membrane into the negative half-cell, which altered the performance of the cell and constituted a limiting factor to its service-life. Nikiforidis et al used a slightly lower concentration of cerium in the positive half-cell electrolyte, 0.59 mol dm^{-3} Ce(IV) and 0.08 mol dm^{-3} Ce(III), in 3.5 mol dm^{-3} MSA, and added 0.8 mol dm^{-3} of Zn(II) mol dm^{-3} to control the migration of zinc ions from the zinc electrolyte. [85] The electrolyte in the negative half-cell consisted of a solution of 2.5 mol dm^{-3} Zn^{2+} in 1.5 mol dm^{-3} MSA, which

is more concentrated that in the previous work. Discharge results for these divided and undivided cells are presented in Table 7.

Undivided cells could solve some of the issues found in divided cells by the use of only one electrolyte containing both redox species. Leung et al prepared a single electrolyte consisting of 0.2 mol dm^{-3} Ce(III), 1.5 mol dm^{-3} Zn(II) and 0.5 mol dm^{-3} of MSA [69,86]. The low acid concentration in this case minimised the HER and facilitated the electrodeposition of zinc. The cerium concentration was also kept low as well as otherwise, the zinc electrodeposition overpotential increased significantly due to competition with Ce(IV) ions at the electrode surface. As shown in Table 7, coulombic and energy efficiencies were higher than those obtained with some divided cells. Nevertheless, the low cerium concentration meant that the cell had a relatively poor energy density (*ca.* 11 W h dm^{-3}).

The use of mixed acid electrolytes has been proposed to solve some of the limitations of the current Zn-Ce RFBs. Xie et al reported an increment of the cerium species solubility and enhanced reversibility of the cerium reaction when a mixture of 2.0 mol dm^{-3} MSA and 0.5 mol dm^{-3} sulphuric acid was used to dissolve 0.3 mol dm^{-3} of Ce(III) [87, 88]. The coulombic and energy efficiencies of this cell are 87.1 % and 73.5 %, respectively. The effect of sulfuric acid on the stability of the carbon-based electrodes in the most advanced laboratory cells has yet to be investigated. On the other hand, mixed acid media can be detrimental to undivided cells, by diminishing the efficiency of both cerium reaction and zinc electrodeposition due to the high proton concentration [86]. Nikiforidis and Daoud [89] recently published a study of hydrochloric, sulfuric and nitric acids for mixed acid electrolytes for the Zn-Ce RFB. These authors reported that the addition of 0.5 mol dm^{-3} of HCl to an electrolyte with 0.6 mol dm^{-3} of

Ce(III) and 4.0 mol dm^{-3} of MSA has an significant positive effect on the reversibility and kinetics of the cerium redox reaction for temperatures ranging from 25 ºC to 55 ºC. While sulfuric acid (0.5 to 2 mol dm^{-3}) in the electrolyte also produced higher exchange current densities and diffusion coefficients, the reversibility of the reaction did not improve. Electrolytes containing nitric acid (0.5 to 2 mol dm^{-3} HNO_3 + 4 M MSA) were found to be unsuitable.

Alternatives to MSA as supporting electrolytes have also been suggested. A Zn-Ce test cell with sulfamic acid media yielded a coulombic efficiency of 90 % [90]. Xie et al presented kinetic data for the cerium reaction in a mixture of sulfosalicylic and sulphuric acid, although this option has not been tested in a flow cell [91]. Modiba et al proposed a different cerium RFB in which cerium in sulphuric acid is used in both half-cells, in a way comparable to the vanadium system [56, 92-94]. This can be achieved by use of cerium species complexed with diethylenetriaminepentaacetic acid (DTPA) in one side of the membrane. The reported improvement of the cerium reaction kinetics when complexed with DTPA suggests that the addition of such complexing agents in Zn-Ce RFBs could prove beneficial. The stability of DTPA and similar substances in MSA electrolytes has to be investigated further though under operational conditions. Preliminary tests by Xie et al showed a positive effect of DTPA [88].

4.3 Electrodes

The composition of electrodes plays a crucial role in the performance of RFBs, particularly in the Zn-Ce system. Electrodes have to withstand strong acid conditions at relatively high temperatures (>50 ºC). In addition, the positive electrode has to operate under the oxidizing power of cerium. Naturally, plates and meshes of noble metals were the first choice of electrode

materials during the early stages of development. Nevertheless, it was also clear that carbon-based materials offered a much cheaper and practical option, either as plates, felts or foams, all of which are widely available in the electrochemical industry. As discussed in the next section, evidence seems to point in the direction of carbon based materials as the best option for the Zn-Ce RFBs. Inevitably, inclusion of polymer particles in composite electrodes decreases the conductivity compared to graphite and may give rise to feeder contact problems [85] but provides a practical, robust carbon-polymer composite for use in larger cells. The use of certain carbon felt electrodes may avoid the need for expensive platinum coatings for positive electrodes but careful choice and preparation of such materials is needed as well as adequate attention to full backplate feeders to distribute the current density as evenly as possible over the 3-D electrode surface.

4.3.1 Positive electrode

Several positive electrode materials have been tested in a divided RFB, including platinized titanium, graphite, carbon polyvinyl ester, reticulated vitreous carbon and carbon felt [34]. Of these, platinized titanium meshes (Pt loading: 70 g m^{-2}) and some carbon felts were found suitable for Zn-Ce RFBs, showing the highest discharge current densities. In these conditions platinized titanium electrodes yielded coulombic and voltage efficiencies of 99.4 % and 59.6 %, respectively, at a current density of 50 mA cm^{-2} (Table 1B). Favourably, the performance of the carbon felt electrodes was very close to the platinum materials, with coulombic and energy efficiencies of 92 % and 63 % respectively. This indicates that certain carbon felts might be used instead of noble metal substrates as positive electrodes, greatly reducing the cost of a Zn-Ce RFB system. A method to improve the binding of the carbon felt to its substrate (graphite plate) has to be found in order to reduce the ohmic loses and increase the durability of the electrode. Carbon felts were used successfully again in an undivided cell, which showed an energy

efficiency of 76 % [69, 86]. The felts were pressed onto a polyvinyl ester-carbon plate. Other examples of carbon felt use can be found in the cells used by Xie et al [87] and Xiong et al [90] for the evaluation of acid electrolyte alternatives. The presence of uncoated parts of carbon electrode surfaces, however, requires care due to possible oxidation. Ce(IV) oxidation of carbon is a key reason titanium sheets were used as current collectors and normally compression was employed to provide contact between the backplate and the 3-D electrode as adhesives suffer from long-term degradation and conductance problems.

Similar results were obtained using platinized titanium mesh as the positive electrode in another divided cell [85]. The highest values for coulombic and energy efficiency were 90 % and 64 %, respectively. It is worth noting that the Pt content was lower (only 10 g m^{-2}) than in the cell mentioned above, yet the performance was almost the same. This indicates that a relatively thin Pt coating is sufficient to provide high current densities, at least in short term trials.

A recent electrochemical evaluation of different Pt-based metallic coatings on Ti substrates as positive electrode materials for the Zn-Ce system suggest that the presence of a Pt-Ir coating increased the kinetics of the Ce(III)/(IV) reaction substantially. This was especially so at elevated temperatures where increases in the exchange density by factors of *ca.* 40 – 100 were measured over the temperature range 25 °C to 60 °C [95, 96]. This was aided in no small part by the large specific electrochemical area of the order of ~100 cm^2 mg^{-1} and ~40 cm^2 mg^{-1} achieved by the Pt-Ir and Pt coatings, respectively. Clearly then, for commercial exploitation,the investigation of practical catalyst-modified carbon felts as positive electrodes is an important research opportunity.

4.3.2 Negative electrode

Nikiforidis et al has published two electrochemical studies of several carbon-based materials as negative electrodes in the Zn-Ce RFB [70, 97]. Carbon-polyvinyl ester, polyvinylidene fluoride, high-density polyethylene, glassy carbon, and graphite foil were considered. It was found that carbon polyvinyl ester-carbon and polyvinylidene fluoride-carbon composites exhibited high coulombic efficiencies and maintained their integrity over more than 200 charge/discharge cycles. These materials were used in flow battery studies, where they exhibited coulombic efficiencies of 90 % and 81 %, respectively [85]. Carbon-polyvinyl ester was superior to polyvinylidene fluoride, with an energy efficiency of 64 % *vs*. 61 %.

One of the major factors impacting on the voltage efficiency (and so energy efficiency) of the RFB in the design used by Nikiforidis et al [85] has been the resistance of the negative electrode. The carbon composite plates are attached to the electrode holder (*e.g.* Ti base plate) using a variety of conducting media (such as Leit-C conductive carbon cement, Plano Gmbh or silver conductive paint, RS Components) and pressure was applied to provide a good ohmic contact. Preparation of the adjoining surfaces, *viz.* via mechanical roughening of the carbon composite and surface oxide film removal of the base plate by acid or other etching procedure has to be carefully carried out in order to ensure that the area resistance of the electrode is of the order of 0.02 Ω cm^2 or less. It may well be that better performance could be achieved by direct thermal bonding of the composites to the base plate.

The divided and undivided cells reported by Leung et al used polyvinyl ester plates as the negative electrode [33, 34, 69, 86]. Zinc electrodeposition on this material was previously studied in a parallel flow cell under different zincate and acid concentrations and over a range of operating parameters [71]. Smooth, hexagonal-like crystalline structures without dendrites were

observed. No degradation was reported during the operation of the divided RFBs, which is in accordance with materials testing carried out by Nikiforidis et al [26].

Some divided cells in the literature have used the convenience of zinc plates as the negative electrode to eliminate any effects from the negative electrode in experiments where the conditions in the positive half-cell were studied [87, 90].

4.4 Operational variables

4.4.1 Temperature

Charge/discharge performance of divided Zn-Ce RFBs shows improvement at relatively elevated temperatures. Cells tested in the temperature range of 25 ºC to 60 ºC showed that voltage and charge efficiencies increase along with temperature [34, 85]. The same effect could be seen with the energy efficiency. After evaluating other parameters, an operating temperature of 50 ºC was selected as the most adequate. The coulombic efficiency fell significantly at the lowest temperature, while the optimal temperature had a different value for each of two negative electrode materials, 55 ºC and 45 ºC for polyvinyl ester and polyvinilydene fluoride composites, respectively. These effects can be explained by faster kinetics and increments in the diffusion coefficient due to a reduction in electrolyte viscosity [95].

The relationship between performance and temperature was quite different for an undivided cell, where charge efficiencies decreased with increasing temperature [69, 86]. The optimum performance of the undivided system was found to be at room temperature (23 ºC), which could prove to be one of the advantages of the undivided cell.

4.4.2 Electrolyte flow rate

Leung et al also investigated electrolyte linear flow velocity in their divided cell (Figure 15) [34]. Current densities for both carbon felt and platinized titanium electrodes increased with flow velocity up to 3.9 cm s^{-1}, with no further increases beyond that velocity. For maximum discharge voltage, the optimum flow velocity was 3.9 cm s^{-1} for carbon felt and 2.6 cm s^{-1} for platinized titanium when used as positive electrodes. The highest energy efficiency was obtained at 7.8 cm s^{-1}.

Electrolyte flow velocities between 7.5 and 13.5 cm s^{-1} were employed in the divided cell by Nikiforidis et al [70, 85]. Under these laminar flow conditions, coulombic and voltage efficiencies showed little variation from values of 90 % and 60 %, respectively. A flow velocity of 10.5 cm s^{-1} was thus chosen for subsequent charge/discharge experiments. Xie et al used a flow velocity of 11.5 cm s^{-1} in their divided cell with a mixed electrolyte [87].

In the undivided cell, the common electrolyte was pumped using a range of flow velocities from 0.64 to 7.0 cm s^{-1} [69]. Further increments in velocity over 2.0 cm s^{-1} yielded insignificant improvements in the discharge potential, due to the large surface area of the carbon felt. A flow velocity of 3.9 cm s^{-1} was preferred, since it showed slightly larger charge efficiency.

4.4.3 Current density

The charge/discharge performance at constant current density was studied in a divided cell using a platinized titanium positive electrode [34]. Current density values of 20, 50 and 80 mA cm^{-2} were evaluated. At 50 mA cm^{-2}, the cell exhibited the highest coulombic efficiency, indicating better mass transport and less interference from secondary reactions. Charging current densities of 10 mA cm^{-2} were used throughout the experiments performed with the cell evaluated at the University of Strathclyde [26, 85]. As shown in Table 7, the overall performance of this cell was very similar to the cell described by Leung et al [34].

4.4.4 Charge conditions and cycle life

There is an important relationship between the charge time and the efficiency of the Zn-Ce RFBs. In the first divided cell it was found that long, 4 h cycles yielded low coulombic and voltage efficiencies, 68.3 % and 62.8 %, respectively, as seen in Table 7 [34]. Charge/discharge cycles of 0.25 h duration performed well up to 57 times, with a coulombic efficiency of 85 % but a voltage efficiency of only 46.2 %. The optimal conditions for coulombic, voltage and energy efficiencies (99 %, 69 %, and 60 %, respectively) were found when a 3 h charge period preceded the 0.25 h cycles, although this limited the overall number of cycles to 25. The battery discharge was limited by the inefficiency of the cerium reaction during the first few cycles. The same research group used charging and discharging times of 0.5 hour for the undivided cell [69].

In a second divided cell, charging times from 2 minutes to 4 hours were evaluated in the flow cell for two different negative electrode materials [85]. In both cases, a decrease in the coulombic efficiency was observed at greater charging times, but voltage efficiency remained the same for each electrode. The highest energy efficiencies were obtained at a charge current

density of 10 mA cm^{-2} for 1 and 2 h when polyvinilydene fluoride-carbon and polyvinyl ester-carbon composites were used as negative electrodes.

5. Scale-up and progression

Most studies regarding the Zn-Ce RFB performance have been carried out with laboratory divided cells. Some results have been presented for undivided and stationary cells. These cells typically used <10 cm^2 although data from 100 cm^2 electrodes have also been reported, as noted above. These have yielded experimental results and data for different electrolytes compositions, electrode materials, and operational conditions. Cells with electrode areas *ca.* 0.25 m^2 and Zn-Ce batteries rated at *ca.* 2 kW and based on stacks of 6 such cells have been tested by Plurion Systems in California and Scotland. Plurion UK pursued pilot scale operation rather than R & D and we are not aware of any published performance data on this proprietary process.

The commercial scale-up of the Zn-Ce flow battery focused on replicating laboratory-scale performance in the first instance. In early trials, the electrode was carbon-HDPE composite, one side of which was coated with titanium and platinum by physical vapour deposition, PVD. Due to corrosion of the carbon and pinholes in the coating, later trials used titanium sheet platinised on the anode surface and Nafion® 212 membrane. A bipolar electrode configuration was used with the Ti-based electrode in an HDPE frame. Each bipolar electrode was fitted with an electrical contact to allow voltage profiles to be measured along the stack. Polymer-coated mild steel end plates were used to compress the <60 electrode cell stack.

The cross-sectional area and electrolyte flow path were informed by CFD modelling to optimize fluid flow across the whole electrode surface, with regard to the changing inter-electrode gap, as zinc was cyclically deposited and stripped. Manifolds were designed on the basis of shunt

current modelling. In the early designs, gaskets, held under compression by steel endplates and tie rods, provided sealing. One stack design is shown in Figure 17 [98], with Figure 17a) showing the overall stack, b) Figure 17b) the components of one cell and Figure 17c) the arrangement of identical cell components in a stack.

Heated/insulated HDPE tanks were used to house the electrolytes. Various trips and alarms were included in the pilot plant to ensure safe operation in the unmanned mode and the overall system was controlled from a custom-built SCADA system. Full-scale experiments showed a similar performance to laboratory scale cells with coulombic efficiencies <80% being possible.

The approximate cell and operational conditions which were typically used for pilot-scale operation at Plurion in Glenrothes are summarized in Table 8. Typically, voltage efficiency exceeded 70 % and a discharge power density of 2 kW m^{-2} was experienced at charge and discharge cell voltages of 2.7 V and 2.1 V. Figure 18 shows typical efficiency data from the Plurion Zn-Ce pilot cell, showing the electrochemical coulombic-, voltage- and energy efficiency at 60 ^{o}C over 23 successive charge-discharge cycles at a current density of 50 mA cm^{-2}. The cerium electrolyte was a 287.5 dm^3 volume of solution containing 0.6 mol dm^{-3} Ce, 1.0 mol dm^{-3} Zn and 3.5 mol dm^{-3} H^+ while the zinc electrolyte was a 187.5 dm^3 volume of solution containing 0.4 mol dm^{-3} Ce, 1.5 mol dm^{-3} Zn and 2.7 mol dm^{-3} H^+. The highest steady cell performance values were 80% coulombic efficiency, 60% voltage efficiency and 45-5% energy efficiency (excluding pumping requirements). It is understood that degradation of the titanium electrode substrate, with the occurrence of corrosion and passivation, was a major problem in long term operation and platinum coated carbon-polymer composites were explored as electrode materials.

It is clear that scale-up to larger electrode areas (ca. 1 m^2), more cells per stack (over 100) and experience with installations using multiple stacks are needed in order to improve confidence in the Zn-Ce battery technology at grid scale level. Computer aided design of moulded polymer frame cell stacks, involving 50+ bipolar electrodes, each ca. 1 m^2 electrode area was realised

during the later stages of development in Plurion but liquidation of the company prevented their realisation.

6. Conclusions and future developments

1. Zn-Ce cell developments have been aided by extensive historical studies of the zinc deposition/stripping and cerium redox half-cell reactions.
2. The Zn-Ce battery chemistry has normally involved aqueous methanesulfonic acid electrolytes in a cell divided by a proton exchange membrane. The attractions of the Zn-Ce cell include a high open-circuit cell potential of *ca.* 2.2 V and a moderately high volumetric energy density (25 – 35 W h dm^{-3}).
3. The kinetics of the cerium half-cell and the cell capacity can be improved by: (i) using a single acid medium in which the cerium salt has a good solubility, (ii) using additives and (iii) using a mixed acid electrolyte.
4. The oxidation of Ce(III) to Ce(IV) takes place at very positive potentials (1.2 V – 1.7 V *vs*. SHE) such that oxygen evolution is a noticeable side-reaction during charging.
5. Selection of a positive electrode material is limited by the need to have a catalytic material for the Ce(IV)/Ce(III) redox reaction together with a high chemical stability of the material in the strong acid electrolytes which contain appreciable levels of the oxidant Ce(IV) during charge. Platinised titanium and platinised carbon have been favoured. Certain uncoated carbon electrodes show possibilities but require further research.
6. The life-time of the of the positive electrode material in the strongly oxidising Ce(IV) electrolyte in the charged condition is limited by surface degradation *viz.*, carbon oxidation (at the interfaces with filler particles in the carbon composites) or slow anodic dissolution of the precious metal coatings. Thick precious metal coatings can provide several years lifetime,

albeit at high cost. Further work on robust, stable carbon materials capable of scale-up is warranted.

7. There are two major problems associated with the zinc electrode. Firstly, zinc deposition and stripping on the negative electrode in the acid medium results in shape change and variation in the electrode-membrane gap. Secondly, a minimisation of the secondary hydrogen evolution reaction at the negative electrode during charge is necessary and loss of the electrodeposited zinc due to corrosion has to be reduced [99]. Electrolyte additives can be used to address to some extent both these problems but further optimisation studies are still required.
8. The great majority of work has involved cells with electrode pairs separated by a proton exchange membrane (typically Nafion® 1100 EW series perfluorocarbon). An undivided cell has recently been introduced at laboratory scale and shown to offer a reasonable performance under restricted operational conditions. Microporous dividers and other ion exchange membranes having lower cost and good lifetime together with appropriate conductivity and transport properties and deserve to be investigated further.
9. Component ageing and degradation during long-term operation requires further study, including corrosion of zinc surfaces and the degradation of carbon electrodes, especially on the positive side.
10. In terms of cell design, 10-100 cm^2 projected area electrode unit cells have been used in the laboratory. For the commercial pilot-plant investigations, bipolar cell stacks with <60 cell and 0.24 m^2 projected electrode area have been employed. Traditional machining of polymer sheets has tended to give way to moulded cell frames at pilot-scale. Very recently, high surface area, porous 3-D electrodes (e.g. felt and foam) and printing of cell bodies and other cell components have become a possibility in the authors' laboratories, transforming the costing, design and maintenance outlook for future cell and stack developments.

11. Multi-physics dynamic models have already been successfully employed on other RFBs. These should also be applicable here to predict the performance and rationalize the importance of operational variables of the Zn-Ce RFB, in terms of the cell voltage variation during multiple charge and discharge cycles.

12. It is clear that for scale-up to larger electrode areas (and so, higher power output), the use of more cells per stack and expertise in full-scale industrial installations using multiple stacks are needed to improve the confidence in the promising Zn-Ce battery technology.

Finally, it is important to recognise the continued progress and development in other redox flow cell technologies (with lower cell voltages) since the introduction of the Zn-Ce battery [1-3]. For example, hydrogen-bromine cells can claim a high power output, albeit with the hazards and environmental problems caused by hydrogen storage, a highly exothermic hydrogen-bromine reaction and also, bromine storage and transport. Detailed mathematical modelling, and developments in the vanadium redox flow batteries (including vanadium-bromine cells and vanadium-hydrogen cells) have led to continuous improvements in electrode materials, membranes and cell monitoring strategies. Although the cells do not require expensive electrocatalysts, there is nevertheless a relatively expensive electrolyte start-up costs required.

Acknowledgements

The authors gratefully acknowledge early contributions to literature searching by Dr Xiaohong Li. The intellectual property rights of the Plurion technology are owned by Scottish Enterprise.

List of symbols

Symbol	Meaning	Units
D	Diffusion coefficient of an ion	$cm^2\ s^{-1}$
E	Electrode potential	V
E_{cell}	Cell potential	V
E_{onset}	Electrode potential for the onset of zinc deposition	V
F	Faraday constant	$C\ mol^{-1}$
ΔG_{cell}	Gibbs free energy change for the cell reaction	$J\ mol^{-1}$
I	Current	A
I_L	Limiting current	A
I_{max}	Maximum current	A
j	Current density	$A\ cm^{-2}$
j_{corr}	Corrosion current density	$A\ cm^{-2}$
k	Rate constant	$cm\ s^{-1}$
k^o	Rate constant under specified conditions	$cm\ s^{-1}$
N_o	Nucleation density for zinc	cm^{-2}
t	Time	s
t_{max}	Time for the maximum current	s
T	Temperature	^oC
v	Mean linear velocity of electrolyte past the electrode surface	$cm\ s^{-1}$

Greek

η_c	Charge efficiency	dimensionless
η_v	Voltage efficiency	dimensionless
ω	Rotation speed of the disc electrode	$rad\ s^{-1}$

Abbreviations

RFB	Redox flow battery

References

1. P.K. Leung, X. Li, C. Ponce de Léon, L. Berlouis, C.T.J. Low, F.C. Walsh, *RSC Advances* **2012**, 2, 10125-10156.

2. M. Skyllas-Kazacos, M.H. Chakrabarti, S.A. Hajimolana, F.S. Mjalli, M. Saleem, *J. Electrochem. Soc*. **2011**, 158, 55-79.

3. A.Z. Weber, M.M. Mench, J.P. Meyers, P.N. Ross, J.T. Gostick, Q.H. Liu, *J. Appl. Electrochem*. **2011**, 41, 1137-1164.

4. C. Ponce de Leon, A. Frias-Ferrer, J. Gonzalez-Garcia, D.A. Szanto, F.C. Walsh, *J. Power Sources* **2006**, 160, 716-732.

5. D. Pletcher, A. Hazza, R.G.A. Wills, Phys. Chem. Chem. Phys. **2004**, 6, 1773..

6. S. Müller, F. Holzer and O. Haas, *J. Applied Electrochem.* **1998**, 28, 895-898.

7. P.K. Leung, Q. Xu, T.S. Zhao, *Electrochim. Acta* **2012**, 79, 117-1258.

8. R.L. Clarke; B.J. Dougherty; S. Harrison; P.J. Millington; S. Mohanta, US 2004/ 0202925 A1, **2004**.

9. J. Garche, C. Dyer, P. Moseley, Z. Ogumi, D. Rand, B. Scrosati, *Encyclopedia of Electrochemical Power Sources*, Elsevier **2009**, 5, 487-496.

10. X. Li, D. Pletcher, C. Ponce-de-León, F.C. Walsh, R.G.A. Wills, "Redox flow batteries for energy storage using zinc electrodes", in C. Menictas, M. Kazacos, T.M. Lim (eds), Advances in batteries for large- and medium-scale energy storage: Applications in power systems and electric vehicles, Woodhead, **2014**.

11. P.C. Symons and P.C. Butler, *Handbook of Batteries*, ed. D. Linden and T. B. Reddy, McGraw-Hill, **2002**, pp 37.

12. P.C. Butler, P.A. Eidler, P.G. Grimes, S.E. Klassen, R.C. Miles, in: D. Linden and T.B. Reddy, Handbook of Batteries, ed., 3rd edn, McGraw-Hill, **2002**, pp 39.

13. H. Van Parys, G. Telias, V. Nedashkivskyi, B. Mollay, I. Vandendael, S. Van Damme, J. Deconinck, A. Hubin, *Electrochim. Acta* **2010**, 55, 20, 5709-5718.

14. P. Guillaume, N. Leclerc, C. Boulanger, J. Lecuire, F. Lapicque, *J. Appl. Electrochem*. **2007**, 37, (11), 1237-1243.

15. J. McBreen, *J. Electroanal. Chem*. **1984**, 168, (1-2), 415-432.

16. Y. Ito, M. Nyce, R. Plivelich, M. Klein, D. Steingart, S. Banerjee, *J. Power Sources* **2011**, 196, 2340..

17. D.J. MacKinnon, R.M. Morrison, J.E. Mouland, P.E. Warren, *J. Appl. Electrochem.* **1990**, 20, 728.

18. C. Tripathy, I.N. Bhattacharya, P. Gopalakrishna, S.C. Das, *Trans. Indian. Inst. Met.* **1998**, 51, 303.

19. B.C. Tripathy, S.C. Das, P. Singh, G.T. Hefter, *J. Appl. Electrochem.* **1999**, 29, 1229-1235.

20. R.L. Clarke, B.J. Dougherty, S. Harrison, J.P. Millington, S. Mohanta, (Plurion Limited) *Load Levelling Battery and Methods Therefore*. US Patent Application 20 040 197 649, **2004**.

21. R.L. Clarke, B.J. Dougherty, S. Harrison, J.P. Millington, S. Mohanta, (Plurion Limited) *Load Levelling Battery and Methods Therefore*. US Patent Application 20 040 197 649, **2004**.

22. .A.Z.Weber, M.M. Mench, J.P. Meyers, P.N. Ross, J.T. Gostick, Q.H. Liu, *J Appl Electrochem*, **2011**, *41*, 1137–1164..

23. D.L. Piron, D. Mathieu, M.D. Amboise. *Can. J. Chem. Eng.* **1981**, 65, 685.

24. D. Linden, T.B. Reddy, Eds *Handbook of Batteries, 3rd Edition,* McGraw-Hill, **1995**.

25. P.K Leung, PhD thesis, University of Southampton (UK), **2011**.

26. G. Nikiforidis, PhD thesis, University of Strathclyde (UK), **2012**.

27 T. Suwa, T.Kuribayashi, N. Tachikawa, Corrosion Engineering*,* **1988***,* 37, 73.

28. T. Vijayabarathi, D. Velayutham, M. Noel, *J. Applied Electrochem.* **2001**, 31, 979-986.

29. V. Devadoss, M. Noel, K. Jararaman, C.A. Basha, *J. Applied Electrochem.* **2003**, 33, 319-323.

30. R.M. Spotnitz, R.P. Kreh, J.T. Lundquist, P.J. Press, *J. Applied Electrochem.* **1990**, 20, 209-215.

31. S. Harrison, A. Theoret, *J. New Mater. Electrochem. Systems* **1999**, 2*,* 1-9.

32. Z. Xie, D. Zhou, F. Xiong, S. Zhang, K. Huang, *J. Rare Earths* **2011**, 29, 567-573.

33. P.K. Leung, C. Ponce de Léon, C.J.T Low, F.C. Walsh, *Electrochim. Acta* **2011**, 56, 2145-2153.

34. P.K. Leung, C. Ponce de Léon, C.J.T. Low, A.A. Shah, F.C. Walsh, *J. Power Sources* **2011**, 196, 5174-5185.

35. B. Fang, S. Iwasa, Y. Wei, T. Arai, M. Kumagai, *Electrochim. Acta* **2002**, 47, 3971-3976.

36. A. Paulenova, S.E. Creager, J.D. Navratil, Y. Wei, *J. Power Sources* **2002**, 109, 431-438.

37. P. Trinidad, C. Ponce de Leon, F.C. Walsh, *J. Environ. Management*. **2008**, 88, 1417-1425.

38. R.L. Clarke, B. Dougherty, S. Harrison, J.P. Millington, S. Mohanta, US Patent 20040197651, (**2004**).

39. R.L. Clarke, B. Dougherty, S. Harrison, J.P. Millington, S. Mohanta, US Patent 2008233484 (A1), (**2008**).

40. R.L. Clarke, B. Dougherty, S. Harrison, J.P. Millington, S. Mohanta, US2004197649 (A1), (**2004**).

41. Y. Liu, X. Xia, H. Liu, *J. Power Sources* **2004**, 130,299-305.

42. K. Kramer, P.M. Robertson, N. Ibl, *J. Appl. Electrochem*. **1980**, 10, 29-36.

43. V. Devadoss, M. Noel, K. Jayaraman, C.A. Basha, *J. Appl. Electrochem*. **2003**, 33, 319-323.

44. R.P. Kreh, R.M. Spotnitz, J.T. Lundquist, *J. Org. Chem.* **1989,** 54, 1526-1531.

45 T. Vijayabarathi, D. Velayutham, M. Noel, *J. Appl. Electrochem*.**2001**, 31, 979-986.

46. E. Bishop, P. Cofré, *J. Analyst* **1981**, 106, 316-322.

47. M. Breiter, P. Delahay, C.W. Tobias, Advances in Electrochemistry and Electrochemical Engineering Vol. 1, Interscience New York, **1961**.

48. D. Pletcher, A First Course in Electrode Processes, The Electrochemical Consultancy, Romsey, **1991**.

49. F.C. Walsh, A First Course in Electrochemical Engineering, Electrochemical Consultancy, Romsey, **1993**.

50. C.M.A. Brett, M.O. Brett, Electrochemistry Principles, Methods and Applications, Oxford University Press, **1993**.

51. V. Devadoss, C.A. Basha, K. Jayaraman, *J. Ind. Eng. Chem. Res.* **2008**, 47, 4607-4616.

52. T.H. Randle, A.T. Kuhn, *J. Chem. Soc. Faraday Trans*. **1983**, 79, 1741-1756.

53. Y. Maeda, K. Sato, R. Ramaraj, T.N. Rao, D.A. Tryk, A. Fujishima, *Electrochim. Acta*.**1999**, 44, 3441-3449.

54. A. Abbaspour, M.A. Mehrgardi, *J. Talanta* **2005**, 67, 579-584.

55. P. Glentworth, B. Wiseall, C.L. Wright, A.J. Mahmood*, J. Inorg. Nucl. Chem*. **1968**, 30, 967-986.

56. P. Modiba, A.M. Crouch, *J. Appl. Electrochem*. **2008**, 38, 1293-1299.

57. D. Pletcher, E.M. Valdes, *Electrochim. Acta* **1988**, 33, 499-507.

58. Y. Wei, B. Fang, T. Arai, M. Kumagai, *J. Appl. Electrochem*. **2005**, 35, 561-566.

59. M. Matheswaran, S. Balaji, S.J. Chung, I.S. Moon, *Bull. Korean Chem. Soc*. **2007**, 28, 1329-1334.

60. T. Raju, C.A. Basha, *J. Ind. Eng. Chem. Res*. **2008**, 47, 8947-8952.

61. P. Guillaume, N. Leclerc, C. Boulanger, J. Lecuire, F. Lapicque, *J. Appl. Electrochem*. **2007**, 37, (11), 1237-1243.

62. B. Kavitha, P. Santhosh, M. Renukadevi, A. Kalpana, P. Shakkthivel, T. Vasudevan, *Surf. Coat. Technol.* **2006**, 201, 3438-3442.

63. R. Ichino, C. Cachet, R. Wiart, *Electrochim. Acta*. **1996**, 41, (7/8), 1031-1039.

64. M. Mouanga, L. Ricq, J. Douglade, P. Berg,*J. Appl. Electrochem*. **2007**, 37, 283-289.

65. T. Boladjieva, M. Monev, A. Tomandi, H. Kronberger, G. Fafilek. *J. Solid State Electrochem*. **2009**, 13, 671-677.

66. R.L. Clarke, B.J. Dougherty, S. Harrison, J.P. Millington, S. Mohanta, US 2006/0063065 A1, **(2005**).

67. J.W. Kim, H.T. Kim, S.M. Park, *J. Electrochem. Soc*. **2004**, 151, C25-C31.

68. http://www.plurionsystems.com/; accessed April **2011**.

69. P. K. Leung, C. Ponce de Leon, F.C. Walsh, *Electrochem. Comm*. **2011**, 13, 770-773.

70. G. Nikiforidis, L. Berlouis, D. Hall and D. Hodgson, *J. Power Sources* **2012**, 206, 497-503.

71. P. K. Leung, C. Ponce de Leon, C.T.J. Low, F.C. Walsh, *Electrochim. Acta* **2011**, 56, 6536-6546.

72. M. Kazacos. M. Skyllas-Kazacos, *J. Electrochem. Soc*. **1989**, 136, 2759-2760.

73. S. Zhong, M. Kazacos, R.P. Burford,M. Skyllas-Kazacos, *J. Power Sources* **1991**, 36, 29-43.

74. C. Cachet, R. Wiart, *Electrochim. Acta*. **1999**, 44, 4743-4751.

75. http://www.sglgroup.com/cms/international/home/index.html, accessed 22nd October **2012**.

76. http://www.bac2.co.uk, accessed January **2013**.

77. http://www.entegris.com/Index.aspx, accessed 22nd October **2012**.

78. L.H. Mendoza-Huízar, C.H. Rios-Reyes, M.G. Gómez-Villegas, *J. Mex. Chem. Soc*. **2009**, 53, (4), 243-247.

79. B.R. Scharifker, G.J. Hills, *Electrochim. Acta* **1983**, 28, 879.

80. K. Marquez, G. Staikov, J.W. Schultze, *Electrochim. Acta* **2003**, 48, 875-882.

81. J. Yu, H. Yang, X. Ai, Y. Chen, *Russian J. Electrochem*. **2002**, 38, 363-367.

82. P.K. Leung, C.T.J. Low, C. Ponce de Leon, F.C. Walsh, *J. Appl. Electrochem*. (**2014***). in preparation.*

83. D. Pletcher, F.C. Walsh, Industrial Electrochemistry, 2nd edn, Blackies, 1990.

84. F.C. Walsh, *Pure Appl. Chem*. **2001**, 73, (12), 1819-1837.

85. G. Nikiforidis, L. Berlouis, D. Hall, D. Hodgson, *J. Power Sources* 2013, 243, 691-698.

86. P.K. Leung, C. Ponce-de-Leon, C.T.J. Low, A.A. Shah, F.C. Walsh, *J. Power Sources* **2011**, 196, 5174-5185.

87. Z. Xie, F. Xiong, D. Zhou, *Energy Fuels* **2011**, 25, 2399-2404.

88. Z. Xie, Q. Liu, Z. Chang, X. Zhang, *Electrochim. Acta* **2013**, 90, 695-704.

89. G. Nikiforidis, W.A. Daoud, *Electrochim. Acta* **2014**, DOI: 10.1016/j.electacta.2014.06.142.

90. F. Xiong, D. Zhou, Z. Xie, Y. Chen, *Appl. Energy* **2012**, 99, 291-296.

91. Z.P. Xie, F.J. Xiong, D.B. Zhou, *Adv. Mater. Res***. 2011**, 279, 451-455.

92. P. Modiba, M. Matoetoe, A.M. Crouch, *Analytical Letters* **2011**, 44, 1967-1975.

93. P. Modiba, M. Matoetoe, A.M. Crouch, *J. Power Sources* **2012**, 205, 1-9.
94. P. Modiba, M. Matoetoe, A.M. Crouch, *Electrochim. Acta* **2013**, 94, 336-343.
95. G. Nikiforidis, L. Berlouis, D. Hall, D. Hodgson, *Electrochim. Acta* **2014**, 115, 621-629.
96. G. Nikiforidis, L. Berlouis, D. Hall, D. Hodgson, *Electrochim. Acta* **2014**, 125, 176-182.
97. G. Nikifordis, L. Berlouis, D. Hall, D. Hodgson, *Electrochim. Acta* **2013** 113, 412-423.
98. S. Clarke, "Some lessons learned from 20 years in redox flow battery R&D", Flow cells for energy storage workshop, 7-8 March 2012, Washington DC, USA, US Department of Energy, Fuel Cells Technology Office, http://www1.eere.energy.gov/hydrogenandfuelcells/wkshp_flow_cell_2012.html; accessed 26 July 2014.
99. P.K. Leung, P. Herrasti, F.J. Recio, C.T.J. Low, C. Ponce de Leon, F.C. Walsh, *J. Applied Electrochem*., **2014**, *in press*.
100. B Fang, S. Iwasa, Y Wei. T. Arai, *Electrochim. Acta* **2002**, 47, 3971-3976.
101. R.A. Bonewitz, G.M. Schmid, *J. Electrochem. Soc*. **1970**, 117, 1367-1372.
102. Z. Galus, R. N.Adams, *J. Phys. Chem*. **1963**, 67, 866-871.
103. R. Greef, H. Aulich, *J. Electroanal. Chem. Interfacial Electrochem*. **1968**, 18, 295-307.
104. P. Kiekens, L. Steen, H. Donche, E. Temmerman, *Electrochim. Acta*, **1981**, 26, 841-845.
105. Y. Maeda, K. Sato, R. Ramaraj, T.N. Rao, D.A. Tryk, A. Fujishima, , **1999**, 44, 3441-3449.
106. A Kuhn, T.H. Randall, *J. Chem. Soc.*, *Faraday Trans.* **1985**, 81, 403-419.
107. G.A. Sacchetto, P. Pastore, G. Favaro, M. Fiorani, *Analytica Chimica Acta* **1992**, 258, 99-
108. P.K. Leung, C. Ponce de Léon, F.C. Walsh, *Electrochim Acta* **2012**, 80, 7-14.

Author & Year	Electrode material	Electrolyte composition	Method of determination	Temperature T / °C	Charge transfer coefficient	Formal potential, E^0_e / V	Diffusion coefficient of Ce(IV), D / $cm^2\ s^{-1}$	Diffusion coefficient of Ce(III), D / $cm^2\ s^{-1}$	Reaction rate constant, k_s / $cm\ s^{-1}$	Exchange current density j_o / $A\ cm^{-2}$	Ref
Bishop et al (1981)	Pt	0.5 M H_2SO_4 0.02 M Ce(III)	RDE	20	0.30 (cath.)	1.22 *vs.* SCE	NG	NG	3.5×10^{-5}	NG	46
	Au	0.5 M H_2SO_4 0.02 Ce(III)			0.16(cath.)	1.12 *vs.* SCE			7.3×10^{-5}		
	GC	0.5 M H_2SO_4 0.02 M Ce(III)			0.49(cath.)	1.23 *vs.* SCE			8.7×10^{-5}		
Bonewitz et al (1970)	Au	1 M H_2SO_4 0.01 M Ce(III) 0.01 M Ce(IV)	LSV	RT	0.65 ±0.06 (anod.)	1.35−1.50 *vs.* SHE	NG	NG	4.0×10^{-4}	NG	101
Fang et al (2002)	GC	0.1 M H_2SO_4 0.01 M Ce(III)	CV	25	NG	1.21 *vs.* Ag/AgCl	NG	NG	NG	NG	100
Galus et al (1963)	Pt	0.5 M H_2SO_4 0.01 M Ce(IV)	RDE	25	0.21(cath.)	NG	NG	NG	3.7×10^{-4}	NG	102
	CP				0.28(cath.)				3.8×10^{-4}		
Greef et al (1968)	Pt	1 M H_2SO_4 $1\times10^{-}4$ M Ce(III) 0.001 M Ce(IV)	RDE	22±1	0.3	NG	3.4×10^{-6}	NG	NG	0.13	103
Kiekens et al (1981)	Au	1 H_2SO_4 0.001 M Ce(III) 0.010 M Ce(IV)	RDE	20.0±0.1	0.33(cath.)	NG	0.34×10^{-5}	NG	2.0×10^{-4}	NG	104
	GC				0.25(cath.)		0.37×10^{-5}		3.2×10^{-4}		
	Ir				0.26(cath.)		0.37×10^{-5}		3.9×10^{-4}		
Kuhn et al (1985)	Pt	0.5 M H_2SO_4 0.012 M Ce(IV) 0.16 **M** Ce(III)	RDE	25	0.2 (cath.)	NG	NG	NG	3.7×10^{-4}	NG	106
					0.4-0.6 (anod.)						
Liu et al (2004)	Pt	1.25 M H_2SO_4 0.4 M Ce(IV)	CV	25	0.132 (cath.)	0.68 *vs.* MSRE	NG	NG	4.1×10^{-4}	NG	33
Maeda et al (1999)	BDD	0.1 M H_2SO_4 0.006 Ce(III)	CV	25	0.28 (anod.)	1.19 *vs.* SCE	NG	1.05×10^{-5}	2.0×10^{-6}	1.9×10^{-6}	105
		0.1 M HNO_3 0.006 Ce(III)			0.27 (anod.)	1.40 *vs.* SCE		0.55×10^{-5}	1.4×10^{-6}	1.4×10^{-6}	
Pletcher et al (1988)	GC	5 M HNO_3 0.030 Ce(III)	CV	18	NG	1.45 *vs.* SCE(anod.)	NG	$6.2\pm0.3\times10^{-6}$	$3.3\pm0.7\times10^{-2}$	NG	57
Randle et al (1983)	Pt	0.5 M H_2SO_4 0.058 Ce(III) 0.007 Ce(IV)	RDE	25	0.59 (anod.)	NG	NG	$5.2\pm0.3\times10^{-6}$	3.5×10^{-5}	NG	52
Sacchetto et al (1992)	Pt	0.5 M H_2SO_4 0.018 M Ce(III)	RDE	NG	0.28(cath.)	1.17 *vs.* SCE	NG	NG	6.3×10^{-4} (cath.)	NG	107
					0.34 (anod.)				11.3×10^{-4} (anod.)		
	Au	0.5 M H_2SO_4 0.018 M Ce(III) 0.018 M Ce(IV)			0.19(cath.)	1.17 *vs.* SHE			21.0×10^{-4} (cath.)		
					0.12(anod.)				14.2×10^{-4} (anod.)		

Table 1A. Selected voltammetry studies for the Ce(III)/Ce(IV) redox couple on inert electrodes in sulphuric acid.

BDD: Boron-doped diamond; CA: Chronoamperometry; CV: Cyclic voltammetry; DTPA: diethylenetriaminepentaacetate; EDTA: Ethylenediaminetetraacetic acid; EIS: Electrochemical impedance spectroscopy; CP: Carbon paste; Gr: Graphite; LSV: Linear sweep voltammetry; MSRE: Mercury sulphate reference electrode; NG: Not given; RDE: Rotating disk electrode; RT: Room temperature; SCE: Saturated calomel electrode; SHE: Standard hydrogen electrode; SSA: Sulfosalicylic acid.

Author & Year	Electrode material	Electrolyte composition	Method of determination	Temperature, T / °C	Diffusion coefficient of Ce(IV), D / cm^2 s^{-1}	Diffusion coefficient of Ce(III), D / cm^2 s^{-1}	Reaction rate constant k_s / cm s^{-1}	Exchange current density, j_o / A cm^{-2}	Ref
Devadoss et a. (2008)	GC	1.0 M MSA 0.152 M Ce(III) 4.0 M MSA 0.152 M Ce(III)	CV	25±1	NG	0.69×10^{-6}	1.65×10^{-3}	NG	51
Leung et al (2011)	Pt	4.0 M MSA 0.8 M Ce(III)	CV	22	NG	0.5×10^{-6}	NG	NG	33
				50		1.52×10^{-6}			
Modiba et al (2012)	Pt	1 M H_2SO_4 0.1 M Ce(IV)	CV EIS	RT	2.4×10^{-6}	NG	1.6×10^{-4}	NG	93
		1 M H_2SO_4 0.1M Ce(IV) 0.03 EDTA			1.3×10^{-6}		1.9×10^{-4}		
		1 M H_2SO_4 0.1 M Ce(IV) 0.03 M DTPA			1.1×10^{-6}		3.1×10^{-4}		
Nikiforidis et al (2013)	Pt	4.5 M MSA 0.8 M Ce(III)	CV	25	4.63×10^{-7}	NG	NG	NG	97
				60	1.32×10^{-7}				
		4.5 M MSA 0.2 M Ce(IV) 0.02 M Ce(III)	LSV EIS	25	NG			0.37 (Tafel) 0.24 (EIS)	
		3.1 M MSA 0.59 M Ce(IV) 0.07 M Ce(III) 0.7 M Zn(II)	RDE	25	2.17×10^{-7}		1.16×10^{-3}	NG	
				60	4.17×10^{-7}		3.42×10^{-3}		
Xie et al (2011)a	Pt	2 M MSA 0.2 M Ce(III) 0.2 M Ce(IV)	LSV RDE CA	25	2.68×10^{-6} (RDE)	NG	0.79×10^{-4}	1.53×10^{-3}	87
					2.56×10^{-6} (CA)				
		2 M MSA 0.75 M H_2SO_4 0.2 M Ce(III) 0.2 M Ce(IV)			5.93×10^{-6} (RDE)		1.48×10^{-4}	2.86×10^{-3}	
					5.87×10^{-6} (CA)				
	Gr	1 M MSA 1 M H_2SO_4 0.2 M Ce(III) 0.2 M Ce(IV)			NG		4.17×10^{-4}	8.05×10^{-3}	
Xie et al (2011)b	Gr	2 M MSA 0.2 M Ce(III) 0.2 M Ce(IV)	CA RDE CV	25	2.56×10^{-6} (CA)	5.37×10^{-6} (CA)	4.06×10^{-4}	9.8×10^{-3}	32
					2.68×10^{-6} (RDE)	5.56×10^{-6} (RDE)			

Xie et al (2011)c	Pt	1 M H_2SO_4 0.005 M Ce(III) 0.005 M Ce(IV) 0.005 M SSA	CV RDE	NG	NG	6.5×10^{-6}	3.2×10^{-4}	NG	91
Xiong et al (2012)	Pt	1 M NH_2SO_3H 0.3 M Ce(III) 0.1 M Ce(IV)	CV	30	NG	5.93×10^{-6}	4.95×10^{-5}	5.95×10^{-4}	90

Table 1B. Selected voltammetry studies for the Ce(III)/Ce(IV) redox couple on platinum or carbon electrodes in electrolytes for RFBs.

BDD: Boron-doped diamond; CA: Chronoamperometry; CV: Cyclic voltammetry; DTPA: diethylenetriaminepentaacetate; EDTA: Ethylenediaminetetraacetic acid; EIS: Electrochemical impedance spectroscopy; CP: Carbon paste; Gr: Graphite; LSV: Linear sweep voltammetry; MSRE: Mercury sulphate reference electrode; NG: Not given; RDE: Rotating disk electrode; RT: Room temperature; SCE: Saturated calomel electrode; SHE: Standard hydrogen electrode; SSA: Sulfosalicylic acid.

Operational parameter	Separation of the Ce redox peak potentials / mV	Ratio of cathodic to anodic peak current
Potential sweep rate / mV s^{-1}		
8	558	0.51
16	557	0.54
32	736	0.50
64	788	0.51
Concentration of methanesulfonic acid / mol dm^{-3}		
1.0	654	0.42
2.0	710	0.43
4.0	738	0.53
5.0	965	0.65
Concentration of cerium (III)methanesulfonate / mol dm^{-3}		
0.1	591	0.32
0.4	632	0.49
0.8	738	0.53
1.0	857	0.53
Temperature of the electrolyte / ^{o}C		
22	738	0.53
30	659	0.54
40	631	0.56
50	619	0.65
60	660	0.62

Table 2. The effect of operational parameters on the separation of the peak potentials and the ratio of peak currents for the Ce(III)/Ce(IV) redox couple. Unless otherwise stated, the temperature of the electrolyte was 22 ^{o}C and the electrolyte contained 0.8 mol dm^{-3} cerium (III) methanesulfonate in 4.0 mol dm^{-3} methanesulfonic acid. The data was estimated from cyclic voltammograms recorded in the potential range from 0 to + 1.9 V *vs.* Ag|AgCl at a potential sweep rate of 50 mV s^{-1}. After Leung et al [33].

Material	Physical properties	Manufacturer	Ref
BMA5 Fluorocarbon polymer	Density: 2.1 g cm^{-3}; in-plane thermal conductivity: 60 W m^{-1} K^{-1}; through-plane electrical resistivity: <1 Ω mm; thermal expansion: 18 µm m^{-1} K^{-1}	Eisenhuth	75
BBP4 Phenolic resin	Density: 2.0 g cm^{-3}; in-plane thermal conductivity: 77 W m^{-1} K^{-1}; through-plane electrical resistivity: <1 Ω mm; thermal expansion: 6 µm m^{-1} K^{-1}.	Eisenhuth	75
C-PPG86 Polypropylene	Density: 1.9 g cm^{-3}; in-plane thermal conductivity: 44 W m^{-1} K^{-1}; through-plane electrical resistivity: <1 Ω mm; thermal expansion: 32 µm m^{-1} K^{-1}.	Eisenhuth	75
Sigracet TF6 Expanded graphite bipolar plate; fluorocarbon polymer	Density: 1.7 g cm^{-3}; in-plane thermal conductivity: 300 W m^{-1} K^{-1}; through-plane electrical resistivity: <10 Ω mm; thermal expansion:–1.5 µm m^{-1} K^{-1}.	SGL Carbon Gmbh	75
PVE Polyvinyl ester bipolar plate material	Density: 1.82 g cm^{-3}; in-plane thermal conductivity: 46 W m^{-1} K^{-1}; through-plane electrical resistivity: <1 Ω mm; thermal expansion 30 µm m^{-1} K^{-1}.	Entegris Inc.	77
C-HDPE-1 Uncured high density polyethylene (1 mm thickness)	Density: 1.97 g cm^{-3}; in-plane thermal conductivity; 20 W m^{-1} K^{-1}.	SGL Carbon Gmbh	75
C-HDPE-1 Uncured high density polyethylene (5 mm thickness)	Density: 1.97 g cm^{-3}; in-plane thermal conductivity: 20 W m^{-1} K^{-1}.	SGL Carbon Gmbh	75
BAC2 Phenolic resin	Conductive polymer - acid-cure version (10-20% carbon).	BAC2 Ltd.	76

Table 3. Physical properties and source of carbon-polymer composite electrode materials used in the Zn-Ce hybrid RFB.

Carbon-polymer composite electrode	E_{onset} *vs.* $Hg|Hg_2SO_4$ / V at various temperatures / °C		
	25	**40**	**60**
C-PVDF	–1.60	–1.58	–1.55
C-PVE	–1.60	–1.57	–1.60
C-HDPE-1	–1.58	–1.58	–1.52
C-HDPE-2	–1.65	–1.60	–1.54
BAC2	–1.69	–1.65	–1.62
C-PE20	–1.59	–1.62	–1.54

Table 4. Effect of temperature on the onset potential for zinc deposition in 1.5 mol dm^{-3} $Zn(CH_3SO_3)_2$ + 5.7 mol dm^{-3} CH_3SO_3H onto various carbon-polymer composite electrodes. Potential sweep rate: 20 mV s^{-1}. After Nikiforidis et al [70].

0.70 mol dm^{-3} Zn(II)		**1.5 mol dm^{-3} Zn(II)**	
*E vs.*Hg|Hg_2SO_4 / V	N_o / 10^6 cm^{-2}	*E vs.*Hg|Hg_2SO_4 / V	N_o / 10^6 cm^{-2}
–1.60	0.9		
–1.625	1.7	–1.58	2.8
–1.65	2.6	–1.59	2.9
–1.675	3.4	–1.61	3.9
–1.70	5.3	–1.63	4.1
–1.725	6.4	–1.64	4.4
–1.75	6.7	–1.66	4.6
–1.80	12.4	–1.68	4.7
		–1.70	6.3

Table 5. Nucleation density of zinc as a function of potential *(vs.* Hg|Hg_2SO_4) for a glassy carbon electrode in 0.7 and 1.5 mol dm^{-3} Zn(II) and 5.7 mol dm^{-3} CH_3SO_3H solution at 60 °C. After Nikiforidis et al [70].

MSA concentration / mol dm^{-3}	**Corrosion current density, j_{corr} / mA cm^{-2}**	**Rate of weight loss / g h^{-1}**	**H_2 evolution rate / cm^3 h^{-1}**
5	571	0.28	83
3	67	0.33	103
2	68	0.33	106
1	48	0.24	77
Zn(II) concentration / mol dm^{-3}			
0	48	0.24	77
0.5	48	0.23	76
1.0	45	0.22	72
2.0	39	0.19	62
Temperature / °C			
22	45	0.22	72
40	49	0.24	85
50	58	0.28	102

Table 6. Dissolution rate of zinc in methanesulfonic acid under various operational conditions. The measurement temperature was 22 °C unless otherwise stated. After Leung et al. [82, 99]

Author & Year	Positive electrode material	Negative electrode material	Anolyte composition / mol dm^{-3}	Catholyte composition / mol dm^{-3}	Temperature, T / °C	Discharge cell potential / V	Mean linear flow velocity / cm s^{-1}	Current density / mA cm^{-2}	% Coulombic efficiency	% Voltage efficiency	Number of cycles	% Energy efficiency	Ref
Divided cells													
Leung et al (2011)	Carbon felt	Polyvinyl ester	0.8 Ce(III) 4.0 MSA	1.5 Zn(II) 1.0 MSA	50	NG	3.9	50	92	NG	*1 (4 h charge/discharge)*	63	86
	Platinized titanium *(70 g m^2 Pt)*	Polyvinyl ester	0.8 Ce(III) 4.0 MSA	1.5 Zn(II) 1.0 MSA	50	1.86	3.9	50	68.3	63	*4 (4 h charge/discharge)*	43	
	Platinized titanium *(70 g m^2 Pt)*	Polyvinyl ester	0.8 Ce(III) 4.0 MSA	1.5 Zn(II) 1.0 MSA	50	1.77	3.9	50	99.4	59.6	*25 (0.25 h charge/discharge after 3 h charge)*	59	
	Platinized titanium *(70 g m^2 Pt)*	Polyvinyl ester	0.8 Ce(III) 4.0 MSA	1.5 Zn(II) 1.0 MSA	50	1.41	3.9	50	85	46	*57* (0.25 h charge/discharge)	39	
Nikiforidis et al (2013)	Platinized titanium *(10 g m^2 Pt)*	Polyvinyl ester	0.08 Ce(III) 0.59 Ce(IV) 3.5 MSA 0.8 Zn(II)	2.5 Zn(II) 1.5 MSA	55	2.05	12	10	90	73	*20 (1 h charge/discharge after 3 h charge)*	64	85
	Platinized titanium *(10 g m^2 Pt)*	Polyvinylidene fluoride	0.08 Ce(III) 0.59 Ce(IV) 3.5 MSA 0.8 Zn(II)	2.0 Zn(II) 1.7 MSA	45	1.92	10.5	10	81	59	*10 (1 h charge/discharge)*	61	
Undivided cells			**Single electrolyte composition / mol dm^{-3}**										
Leung et al (2011)	Carbon felt	Polyvinyl ester	1.5 Zn(II) 0.2 Ce(III) 0.5 MSA		25	2.34	3.9	20	90	87	10 *(0.5 h charge/discharge)*	76	69
Leung et al (2012)	Carbon felt	Polyvinyl ester	1.5 Zn(II) 0.2 Ce(III) 0.5 MSA		25	2.34	3.9	20	82	NG	10 *(0.5 h charge/discharge)*	72	108

Table 7. The typical discharge performance of divided and undivided cells.

Property	Size
Number of bipolar electrodes	<60
Electrode size	0.4 m × 0.6 m
Projected electrode area	0.24 m^2
Positive (Ce) electrode material	Platinised titanium mesh
Negative (Zn) electrode material	1 mm thick titanium sheet
Positive (Ce) electrolyte	0.6 mol dm^{-3} Ce 0.1 mol dm^{-3} Zn^{2+} 3.5 mol dm^{-3} H^+
Negative (Zn) electrolyte	0.4 mol dm^{-3} Ce 1.5 mol dm^{-3} Zn^{2+} 2.7 mol dm^{-3} H^+
Inter-electrode gap	2.5 mm
Electrolyte temperature	60 ^oC
Mean linear velocity of electrolyte past the electrode surface	10 cm s^{-1}

Table 8. Typical cell characteristics and operational conditions used in the Plurion pilot-scale operation.

Figure captions

Figure 1. The main species and electrode reactions in a proton-membrane divided Zn-Ce flow battery on charge. After Li et al. [10].

Figure 2. A time-line highlighting studies involving the Zn-Ce flow battery.
Plurion closed late 2010/early 2011.

Figure 3. Cyclic voltammograms for the Ce(III)/Ce(IV) redox couple in 0.8 mol dm^{-3} cerium (III) methanesulfonate in 4.0 mol dm^{-3} methanesulfonic acid at 22 ^{o}C at (a) platinum and (b) glassy carbon electrodes. The electrode potential was swept from 0 to + 1.9 V *vs.* Ag|AgCl then from + 1.9 to 0 V *vs.* Ag|AgCl at 50 mV s^{-1}. After Leung et al [33].

Figure 4. The effect of potential sweep rate on the Ce(III)/Ce(IV) redox couple in methanesulfonic acid. (a) Cyclic voltammogram and (b) Randles-Sevćik plot. Electrolyte: as in Figure 3. The potential sweep rates were 8, 11, 16, 22.6, 32, 45.3 and 64 mV s^{-1}. ■ oxidation of Ce(III) and □ reduction of Ce(IV). After Leung et al [33].

Figure 5. The effect of methanesulfonic acid on (a) oxidation of Ce(III) to Ce(IV): (A) 2, (B) 2.5, (C) 3, (D) 4, (E) 4.5 and (F) 5 mol dm^{-3} CH_3SO_3H, respectively, (b) oxygen evolution at platinum without Ce(III) ions: (A) 1, (B) 2, (C) 3, (D) 4 and (E) 5 mol dm^{-3} CH_3SO_3H, respectively and (c) charge density for Ce(III)/Ce(IV) redox couple. Other electrolyte conditions were similar to those in Figure 3. ■ oxidation of Ce(III) and □ reduction of Ce(IV). After Leung et al [33].

Figure 6. The effect of Ce(III) concentration on the charge density of the Ce(III)/Ce(IV) redox couple in methanesulfonic acid. Other electrolyte conditions: as in Figure 3. The charge density was calculated from the area under the cyclic voltammograms between 0 to + 1.9 V *vs.* Ag|AgCl at 50 mV s^{-1}. ■ Oxidation of Ce(III) and □ reduction of Ce(IV). After Leung et al [33].

Figure 7. The effect of electrolyte temperature on the charge density for Ce(III)/Ce(IV) redox couple. Other electrolyte conditions: as in Figure 3. The charge density was calculated from the area under the cyclic voltammograms between 0 to +1.9 V *vs.* Ag|AgCl at 50 mV s^{-1}. ■ Oxidation of Ce(III) and □ reduction of Ce(IV). After Leung et al [33].

Figure 8 Cyclic voltammetry of zinc deposition and dissolution at carbon-polymer composite electrodes. a) C-HDPE composite electrode in 100 mmol dm^{-3} Zn^{2+} + 0.25 mol dm^{-3} $NaCH_3SO_3$ at 298 K. Potential sweep rate: 50 mV s^{-1}; b) C-PVDF composite electrode in a 1.8 M solution of Zn^{2+} + 5.7 M MSA at 60 °C. Potential sweep rate: 20 mV s^{-1}. After Nikiforidis et al. [70].

Figure 9. Koutecky-Levich (*$1/j_L$ vs. $1/\omega^{1/2}$*) plots at a C-PVDF composite electrode for the Zn(II)/Zn(0) couple in 0.01 mol dm^{-3} Zn(II) and 0.25 mol dm^{-3} $Na(CH_3SO_3)$ at 40 °C. Potential: △ =–1.64 V; ×- –1.66 V; ✱ = –1.68 V; ● = –1.70 V; + = –1.72 V; ◆ = –1.74 V; - = –1.76 V; ■ = –1.78 V; ↕ = –1.80 V; ◇ = –1.82 V. After Nikiforidis et al. [70].

Figure 10. Normalised experimental current *vs.* time plots: (a) at –1.68 V vs. $Hg|Hg_2SO_4$ (sat) for zinc electrodeposition from 0.05 mol dm^{-3} Zn(II) in 0.125 mol dm^{-3} $NaCH_3SO_3$ at 30 °C at a PPG86 composite carbon-polymer electrode; b) at –1.65 V for zinc electrodeposition in 0.7 mol dm^{-3} Zn(II) and 5.7 mol dm^{-3} MSA at 60 °C on a glassy carbon electrode. Simulated curves for instantaneous and progressive nucleation are also shown**.** After Nikiforidis et al. [70].

Figure 11. Potential-time responses to galvanostatic charge/discharge cycles for the BAC2 electrode in 1.5 mol dm^{-3} Zn(II) and 5.7 mol dm^{-3} CH_3SO_3H at 30 °C. Charged for 20 minutes at 50 mA cm^{-2}. After Nikiforidis et al. [70].

Figure 12. Charge efficiency at various carbon substrates in 1.5 mol dm^{-3} Zn(II) and 5.7 mol dm^{-3} CH_3SO_3H solution at 60 °C. Charged at –50 mA cm^{-2} for 1 minute; discharged at 50 mA cm^{-2}. After Nikiforidis et al. [70].

Figure 13. Charge efficiency at a C-PVDF composite RDE *vs.* number of cycles at 60 °C, showing the impact of zinc deposition time at 50 mA cm^{-2} in 2 mol dm^{-3} Zn^{2+} and 5.7 mol dm^{-3} MSA. w = 10 Hz. Deposition time: ◇ = 6 s; □ = 120 s; ○ = 300 s; ◆ = 600 s; △ = 1200 s; × = 2400 s. After Nikiforidis et al. [70].

Figure 14. The effect of discharge current density on charge efficiency using a C-PVDF composite electrode at 60 °C following charging for 10 minutes at 50 mA cm^{-2} in 2 mol dm^{-3} Zn^{2+} and 5.7 mol dm^{-3} MSA. Discharge current density: ○= 25 mA cm^{-2}; △ = 50 mA cm^{-2}; □ = 100 mA cm^{-2}; ◇ = 150 mA cm^{-2}. After Nikiforidis et al [70].

Figure. 15. Experimental arrangement and electrical circuit for a divided zinc cerium redox flow battery. (a) Overall set-up showing the points of measurement of the cell potential E_{cell}, the potential of the positive (E_{Ce}) and negative (E_{Zn}) electrodes, and the ohmic voltage drop across the membrane (E_{IR}) and (b) an expanded view of the components of a flow battery. Dimensions are in mm. [86]

Figure. 16. Schematic diagram of the undivided zinc–cerium RFB. (a) experimental arrangement and electrical circuit, (b) the expanded view of the cell components; dimensions are shown in mm. [34].

Figure 17. A Plurion Zn-Ce pilot flow cell stack design having a nominal rating of 0.25 kA and 0.5 kW. a) overall, external view. b) components of one cell, which uses titanium sheet electrodes of approximate size 60 cm x 40 cm and c) the arrangement of identical cell components in a stack. After AIC. [98].

Figure 18. Efficiency data from the Plurion Zn-Ce pilot cell, showing the electrochemical coulombic-, voltage- and energy efficiency over 23 successive charge-discharge

cycles at a current density of 50 mA cm^{-2} and a temperature of approx. 60 ^{o}C. The cerium electrolyte was a 287.5 dm^3 volume of solution containing 0.6 mol dm^{-3} Ce, 1.0 mol dm^{-3} Zn and 3.5 mol dm^{-3} H^+ while the zinc electrolyte was a 187.5 dm^3 volume of solution containing 0.4 mol dm^{-3} Ce, 1.5 mol dm^{-3} Zn and 2.7 mol dm^{-3} H^+.

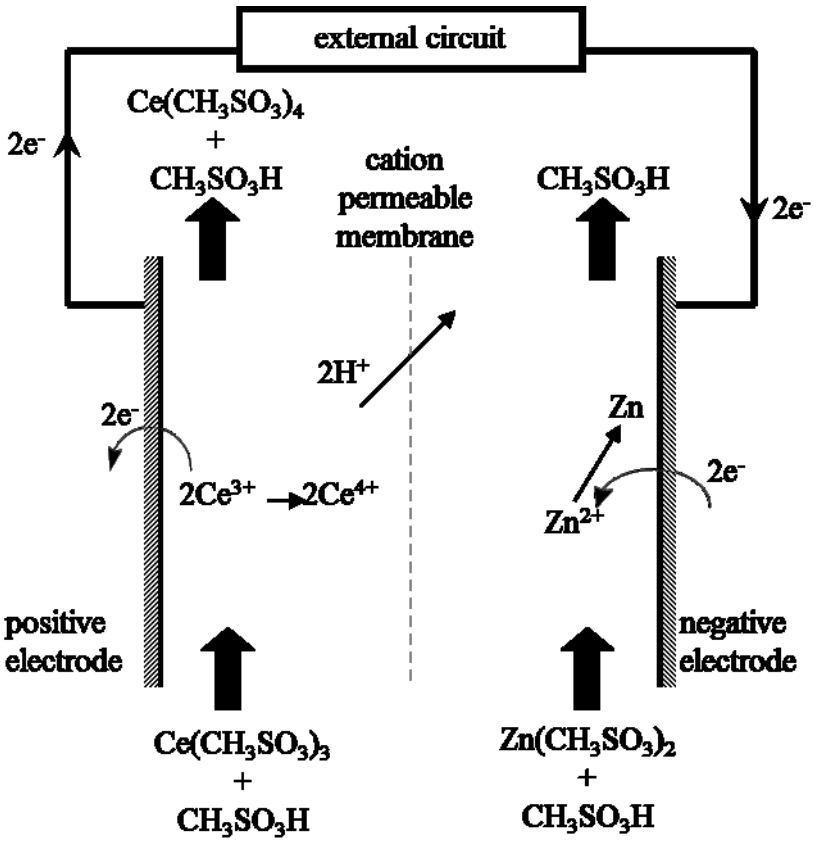
external circuit
Ce(CH3SO3)4
+
CH3SO3H
2e-
cation
permeable
membrane
CH3SO3H
2e-
2H+
2e-
2Ce3+ → 2Ce4+
Zn
2e-
Zn2+
positive
electrode
negative
electrode
Ce(CH3SO3)3
+
CH3SO3H
Zn(CH3SO3)2
+
CH3SO3H

Figure 1.

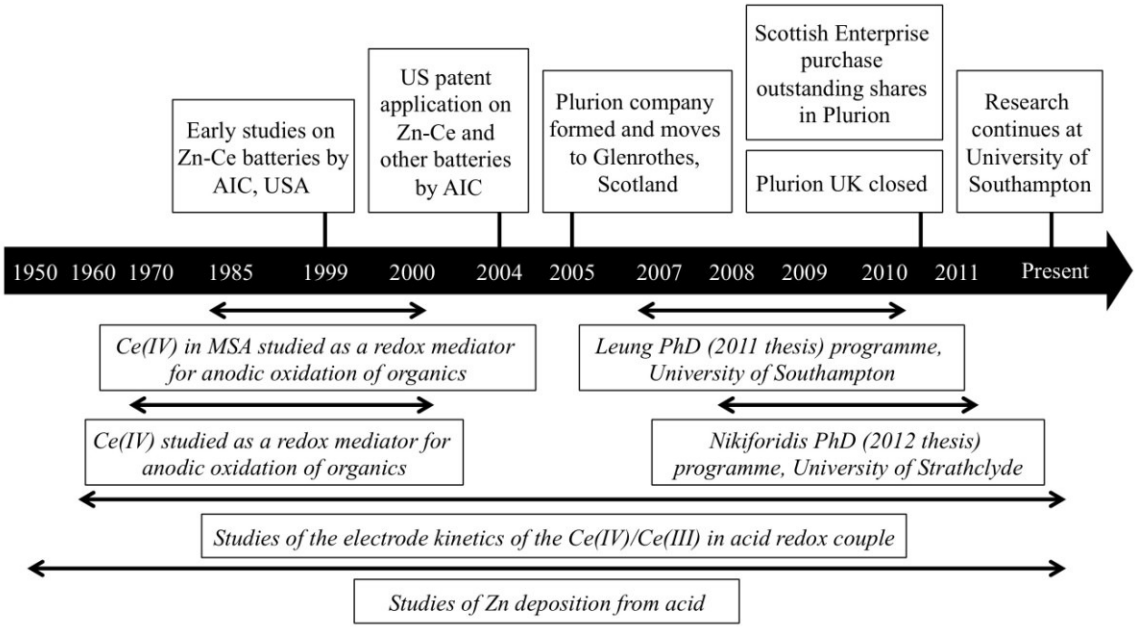
Early studies on Zn-Ce batteries by AIC, USA
US patent application on Zn-Ce and other batteries by AIC
Plurion company formed and moves to Glenrothes, Scotland
Scottish Enterprise purchase outstanding shares in Plurion
Plurion UK closed
Research continues at University of Southampton
1950 1960 1970 1985 1999 2000 2004 2005 2007 2008 2009 2010 2011 Present
Ce(IV) in MSA studied as a redox mediator for anodic oxidation of organics
Leung PhD (2011 thesis) programme, University of Southampton
Ce(IV) studied as a redox mediator for anodic oxidation of organics
Nikiforidis PhD (2012 thesis) programme, University of Strathclyde
Studies of the electrode kinetics of the Ce(IV)/Ce(III) in acid redox couple
Studies of Zn deposition from acid

Figure 2.

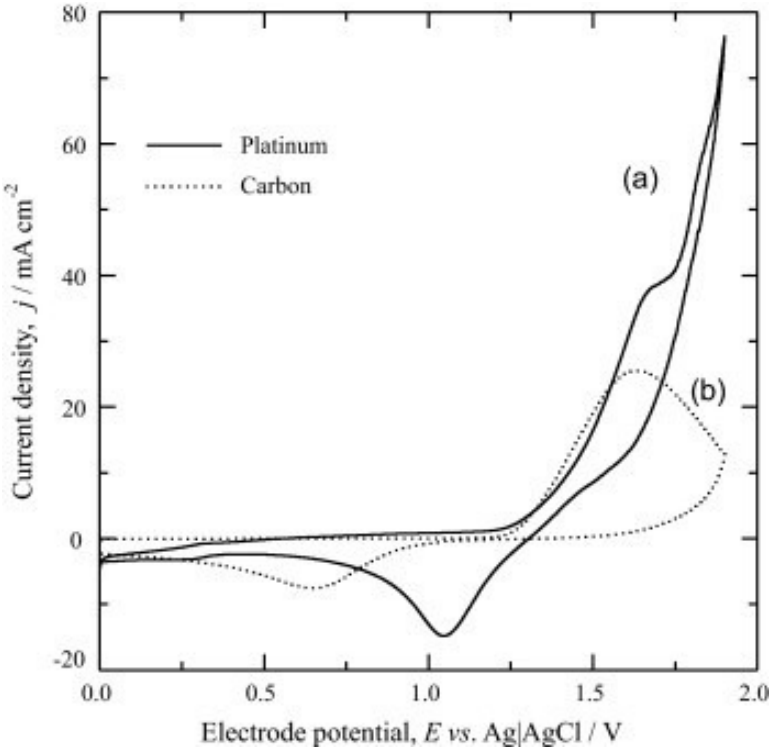
Platinum
Carbon
(a)
(b)
Current density, j / mA cm-2
Electrode potential, E vs. Ag|AgCl / V
80
60
40
20
0
-20
0.0
0.5
1.0
1.5
2.0

Figure 3.

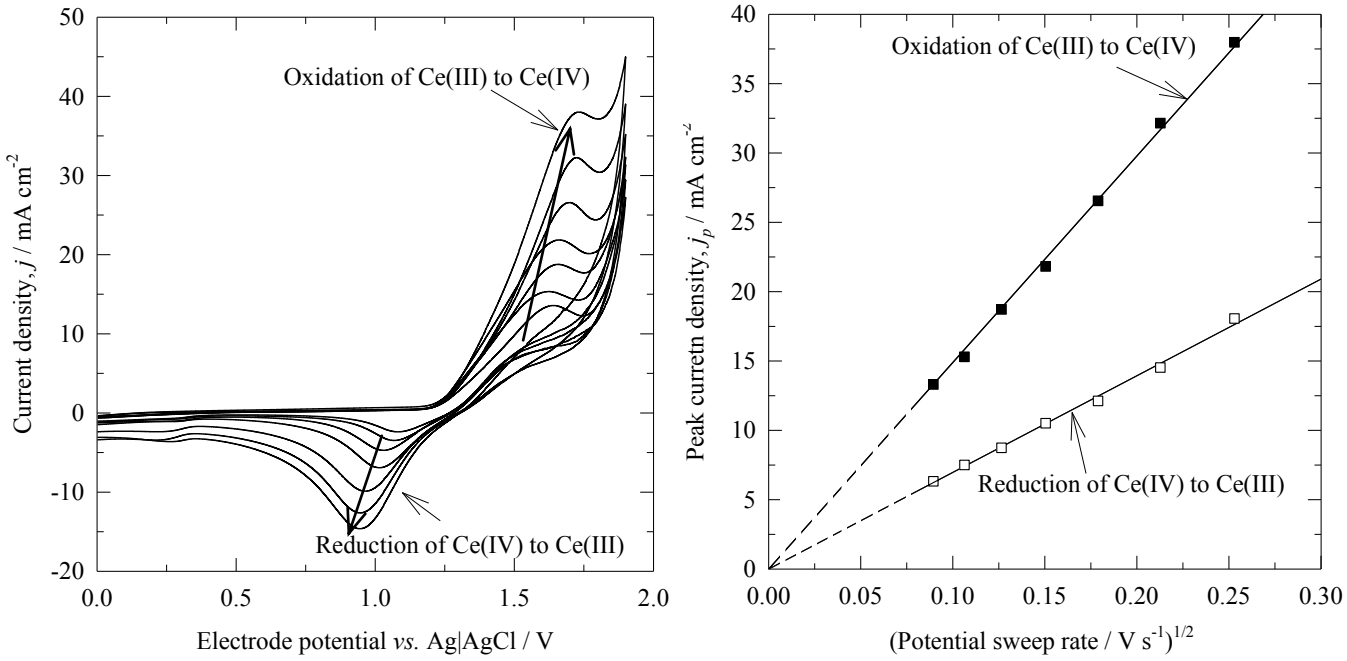
Oxidation of Ce(III) to Ce(IV)
Reduction of Ce(IV) to Ce(III)
Current density, j / mA cm^{-2}
Electrode potential *vs.* Ag|AgCl / V
Peak curretn density, j_p / mA cm^{-2}
(Potential sweep rate / V s^{-1})$^{1/2}$
(a)
(b)

Figure 4.

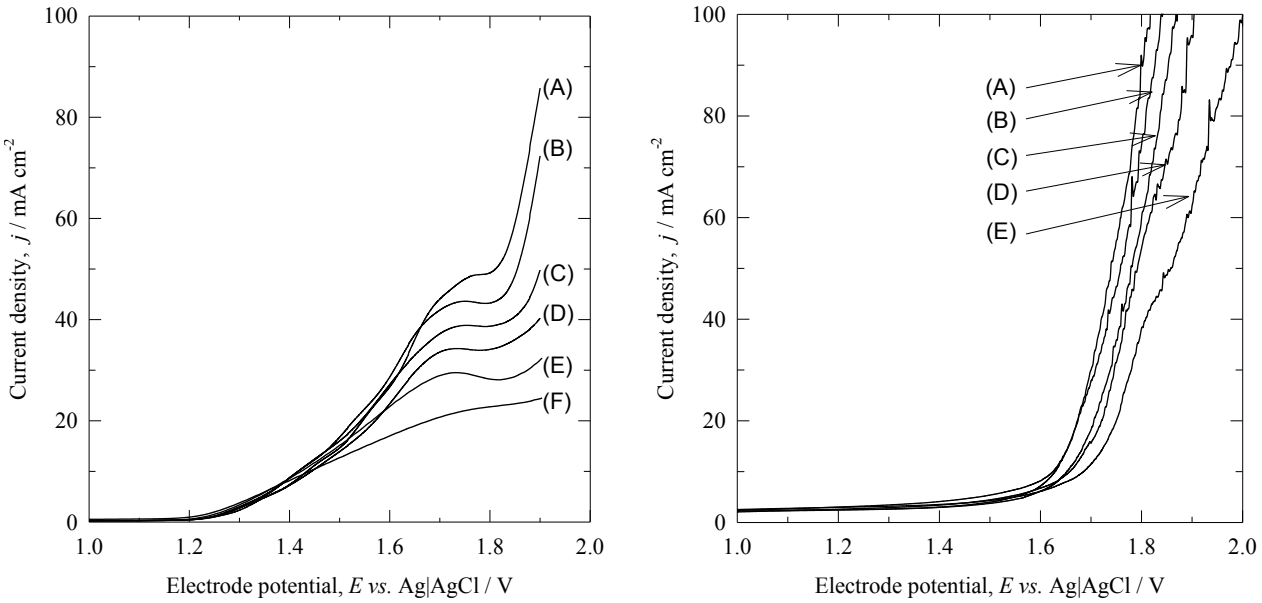
Current density, j / mA cm^{-2}
Electrode potential, E *vs.* Ag|AgCl / V
(A)
(B)
(C)
(D)
(E)
(F)

(a) **(b)**

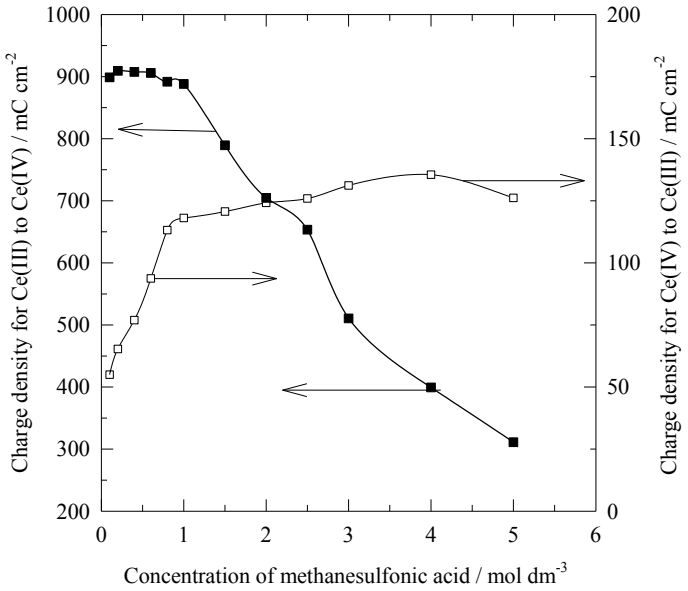
Charge density for Ce(III) to Ce(IV) / mC cm^{-2}
Charge density for Ce(IV) to Ce(III) / mC cm^{-2}
Concentration of methanesulfonic acid / mol dm^{-3}

(c)

Figure 5.

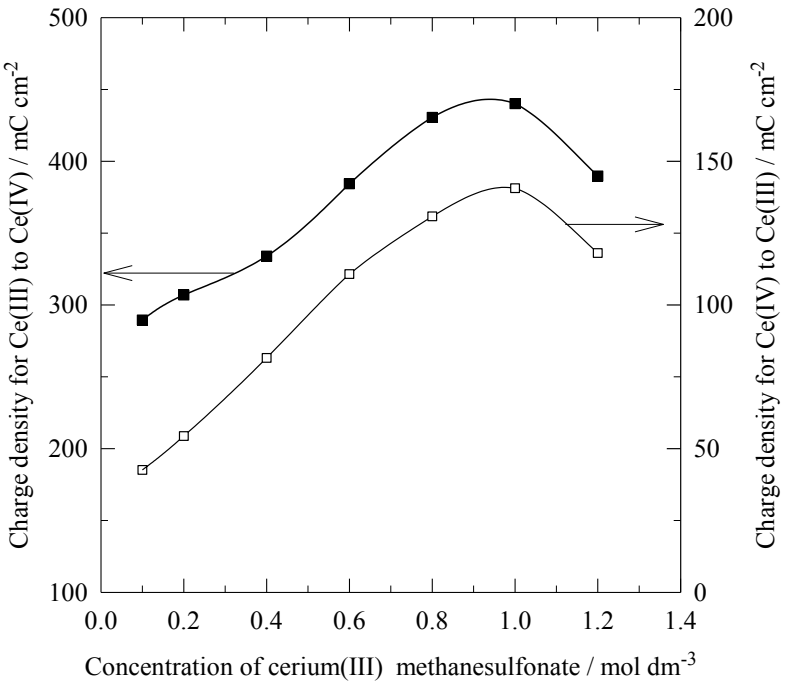
Charge density for Ce(III) to Ce(IV) / mC cm-2
Charge density for Ce(IV) to Ce(III) / mC cm-2
Concentration of cerium(III) methanesulfonate / mol dm-3
500
400
300
200
100
200
150
100
50
0
0.0
0.2
0.4
0.6
0.8
1.0
1.2
1.4

Figure 6.

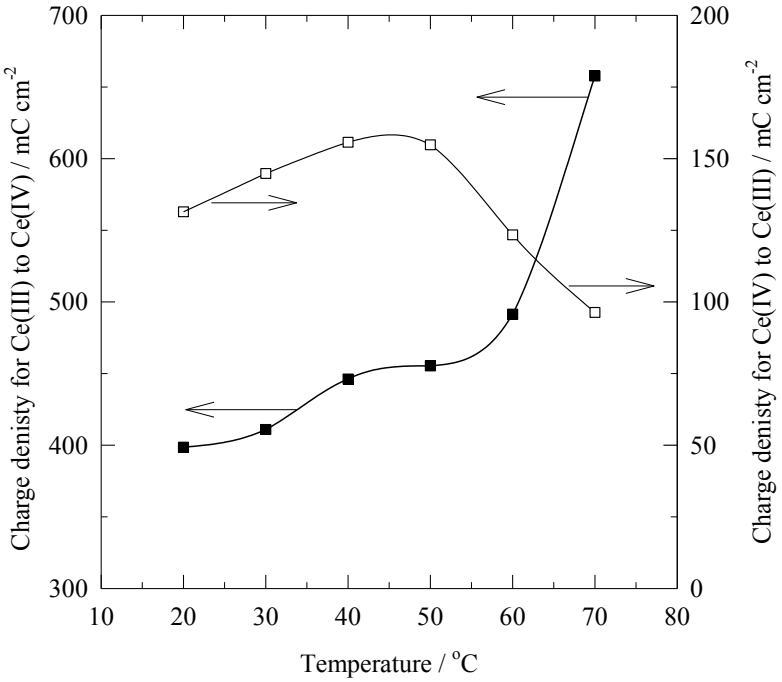
700
600
500
400
300
200
150
100
50
0
10
20
30
40
50
60
70
80
Charge denisty for Ce(III) to Ce(IV) / mC cm-2
Charge denisty for Ce(IV) to Ce(III) / mC cm-2
Temperature / °C

Figure 7.

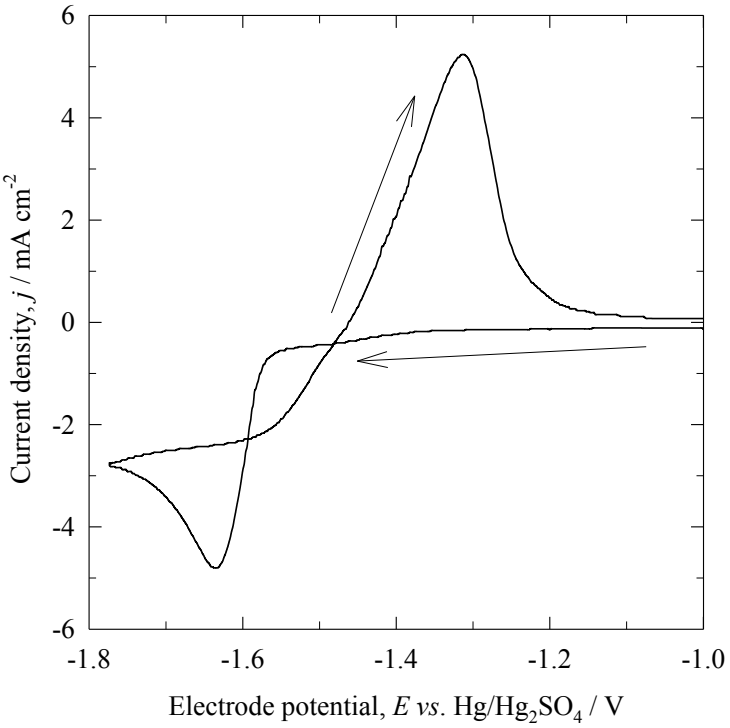
6
4
2
0
-2
-4
-6
-1.8
-1.6
-1.4
-1.2
-1.0
Current density, j / mA cm^{-2}
Electrode potential, E *vs*. Hg/Hg_2SO_4 / V

Figure 8a)

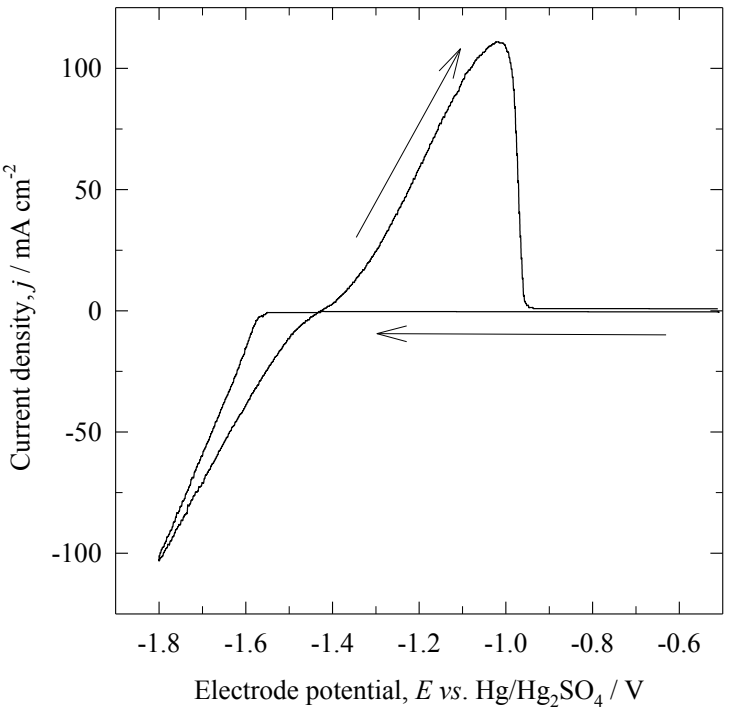
100
50
0
-50
-100
-1.8
-1.6
-1.4
-1.2
-1.0
-0.8
-0.6
Current density, j / mA cm^{-2}
Electrode potential, E *vs*. Hg/Hg_2SO_4 / V

Figure 8b)

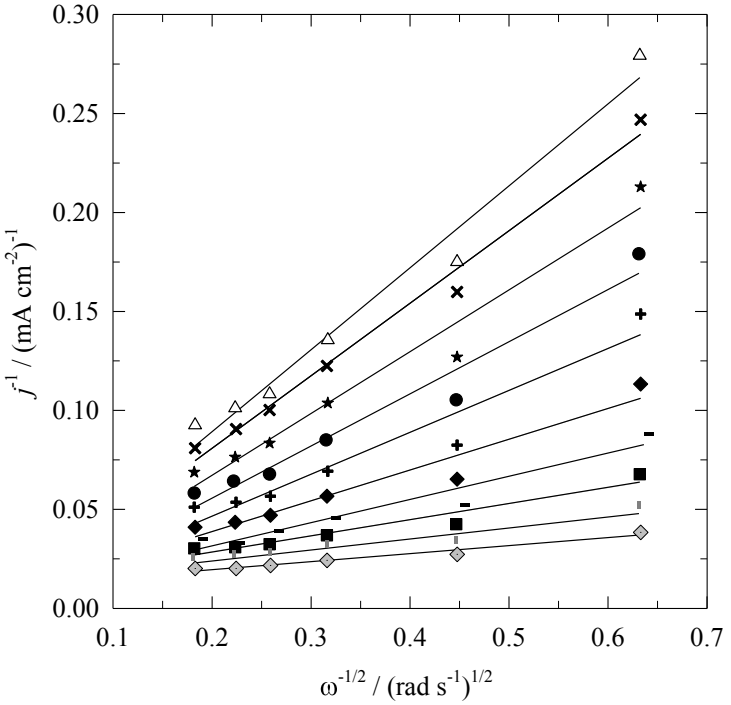
0.30
0.25
0.20
0.15
0.10
0.05
0.00
0.1
0.2
0.3
0.4
0.5
0.6
0.7
j^{-1} / (mA cm^{-2})$^{-1}$
$\omega^{-1/2}$ / (rad s^{-1})$^{1/2}$

Figure 9

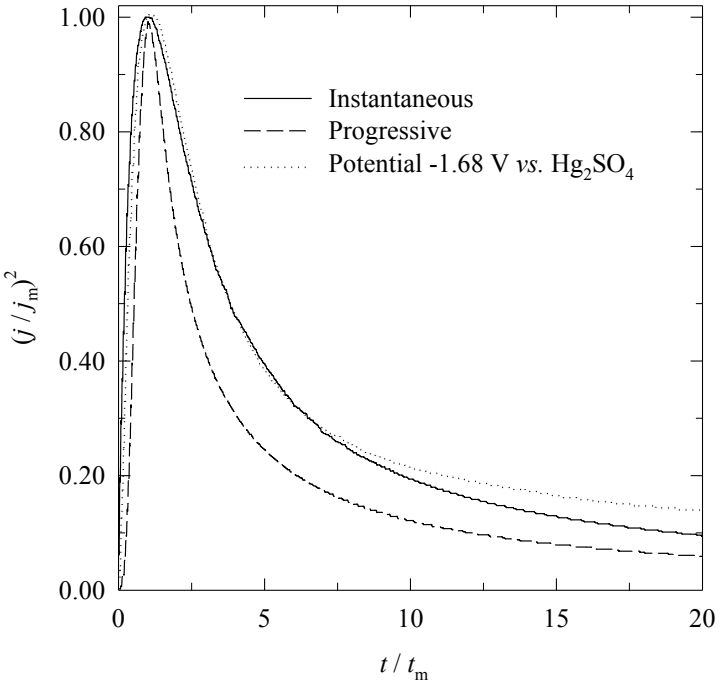
1.00
0.80
0.60
0.40
0.20
0.00
0
5
10
15
20
$(j / j_m)^2$
t / t_m
Instantaneous
Progressive
Potential -1.68 V *vs.* Hg_2SO_4

Figure 10a)

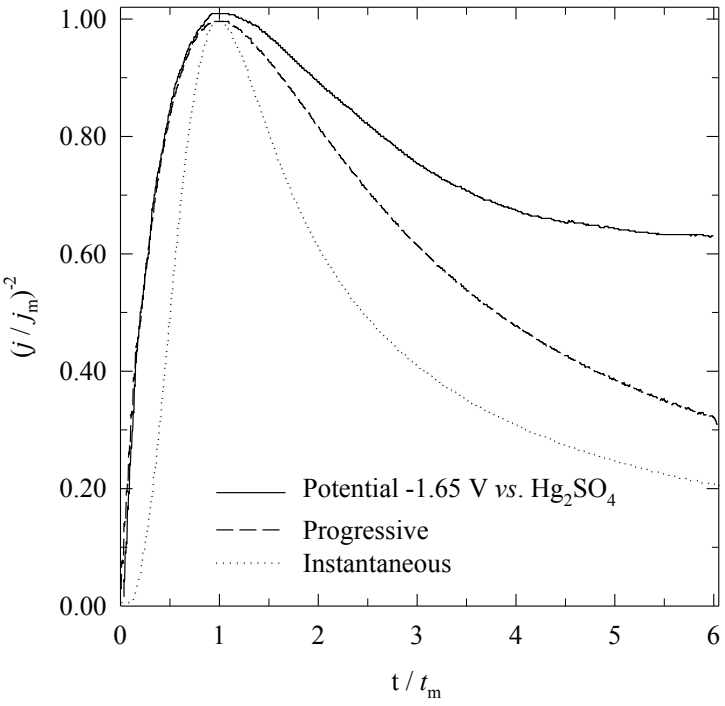
1.00
0.80
0.60
0.40
0.20
0.00
0
1
2
3
4
5
6
$(j / j_m)^{-2}$
t / t_m
Potential -1.65 V *vs*. Hg_2SO_4
Progressive
Instantaneous

Figure 10b)

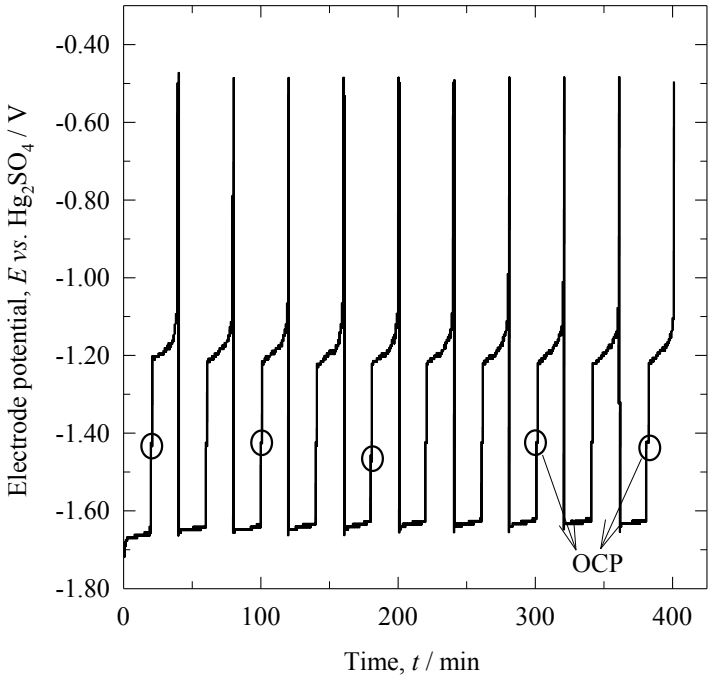
-0.40
-0.60
-0.80
-1.00
-1.20
-1.40
-1.60
-1.80
0
100
200
300
400
OCP
Electrode potential, E vs. Hg2SO4 / V
Time, t / min

Figure 11.

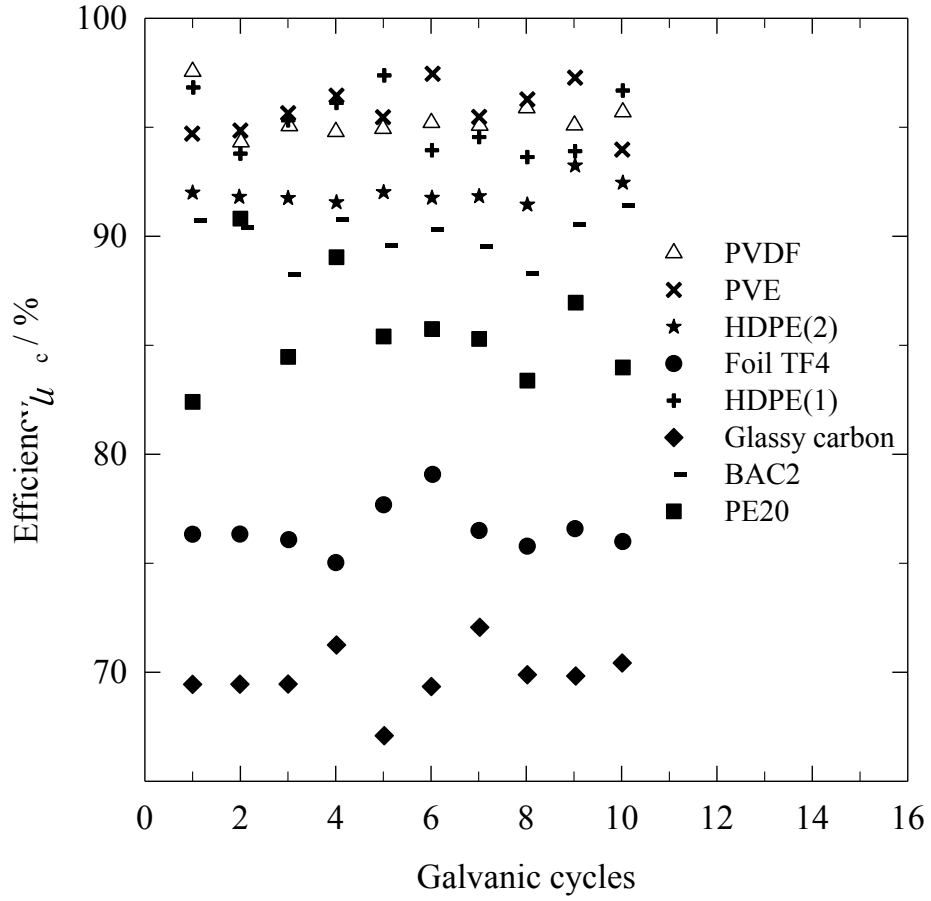
100
90
80
70
0
2
4
6
8
10
12
14
16
Galvanic cycles
Efficiency / %
PVDF
PVE
HDPE(2)
Foil TF4
HDPE(1)
Glassy carbon
BAC2
PE20

Figure 12.

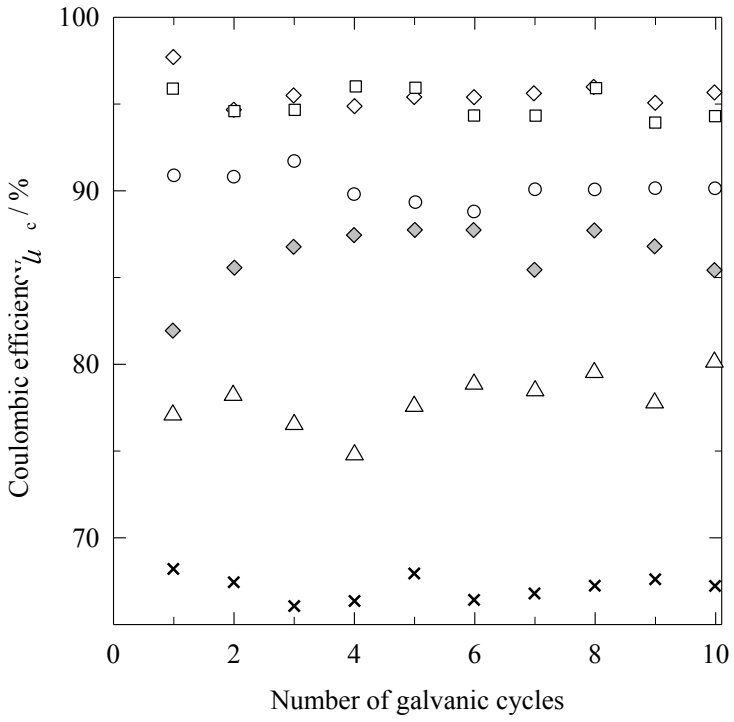
100
90
80
70
0
2
4
6
8
10
Coulombic efficiency η_c / %
Number of galvanic cycles

Figure 13.

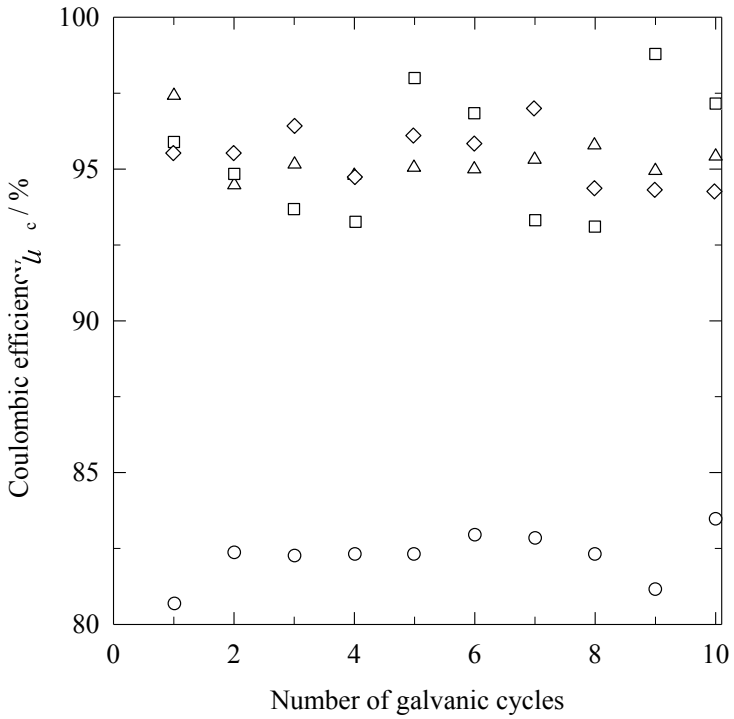
100
95
90
85
80
0
2
4
6
8
10
Coulombic efficiency η_c / %
Number of galvanic cycles

Figure 14.

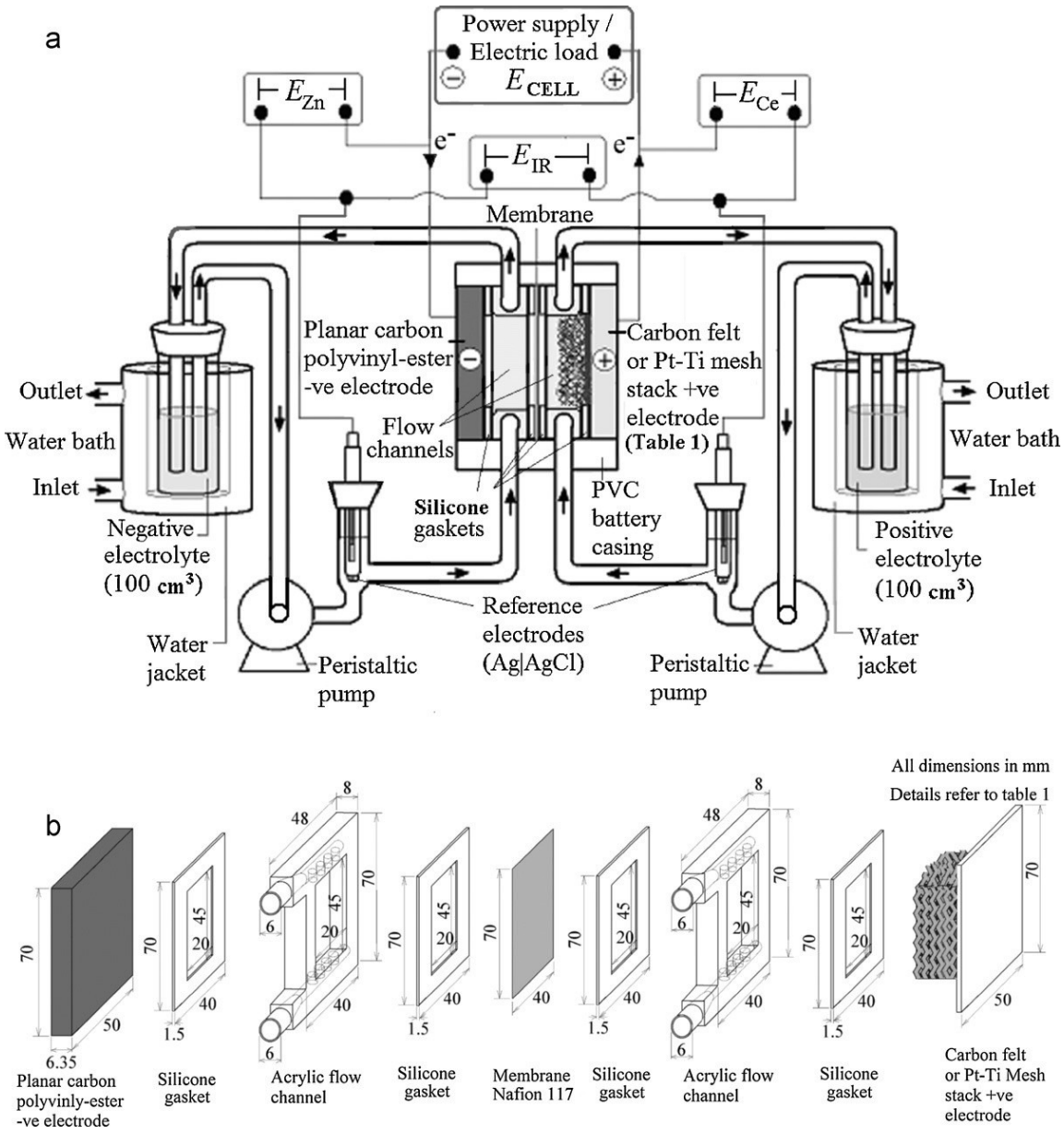
a
Power supply /
Electric load
E_{CELL}
E_{Zn}
E_{Ce}
E_{IR}
e⁻
e⁻
Membrane
Planar carbon polyvinyl-ester -ve electrode
Carbon felt or Pt-Ti mesh stack +ve electrode (Table 1)
Flow channels
Silicone gaskets
PVC battery casing
Outlet
Water bath
Inlet
Negative electrolyte (100 cm³)
Positive electrolyte (100 cm³)
Reference electrodes (Ag|AgCl)
Water jacket
Peristaltic pump
b
All dimensions in mm
Details refer to table 1
Planar carbon polyvinly-ester -ve electrode
Silicone gasket
Acrylic flow channel
Membrane Nafion 117
Carbon felt or Pt-Ti Mesh stack +ve electrode

Figure 15

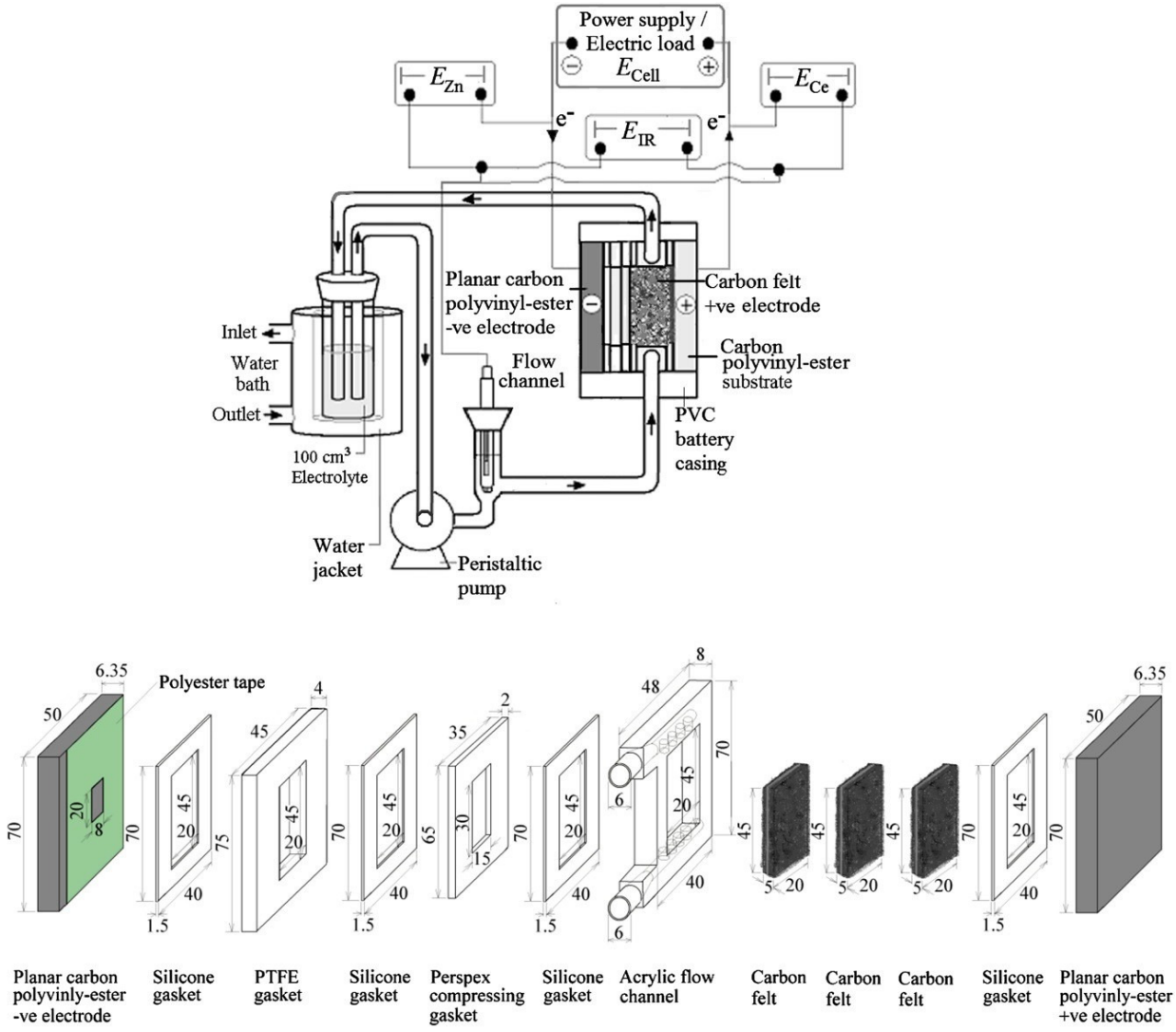
Power supply /
Electric load
E_{Cell}
E_{Zn}
E_{Ce}
E_{IR}
e⁻
e⁻
Planar carbon polyvinyl-ester -ve electrode
Carbon felt +ve electrode
Carbon polyvinyl-ester substrate
Flow channel
PVC battery casing
Inlet
Water bath
Outlet
100 cm³ Electrolyte
Water jacket
Peristaltic pump
Polyester tape
Planar carbon polyvinly-ester -ve electrode
Silicone gasket
PTFE gasket
Silicone gasket
Perspex compressing gasket
Silicone gasket
Acrylic flow channel
Carbon felt
Carbon felt
Carbon felt
Silicone gasket
Planar carbon polyvinly-ester +ve electrode

Figure 16

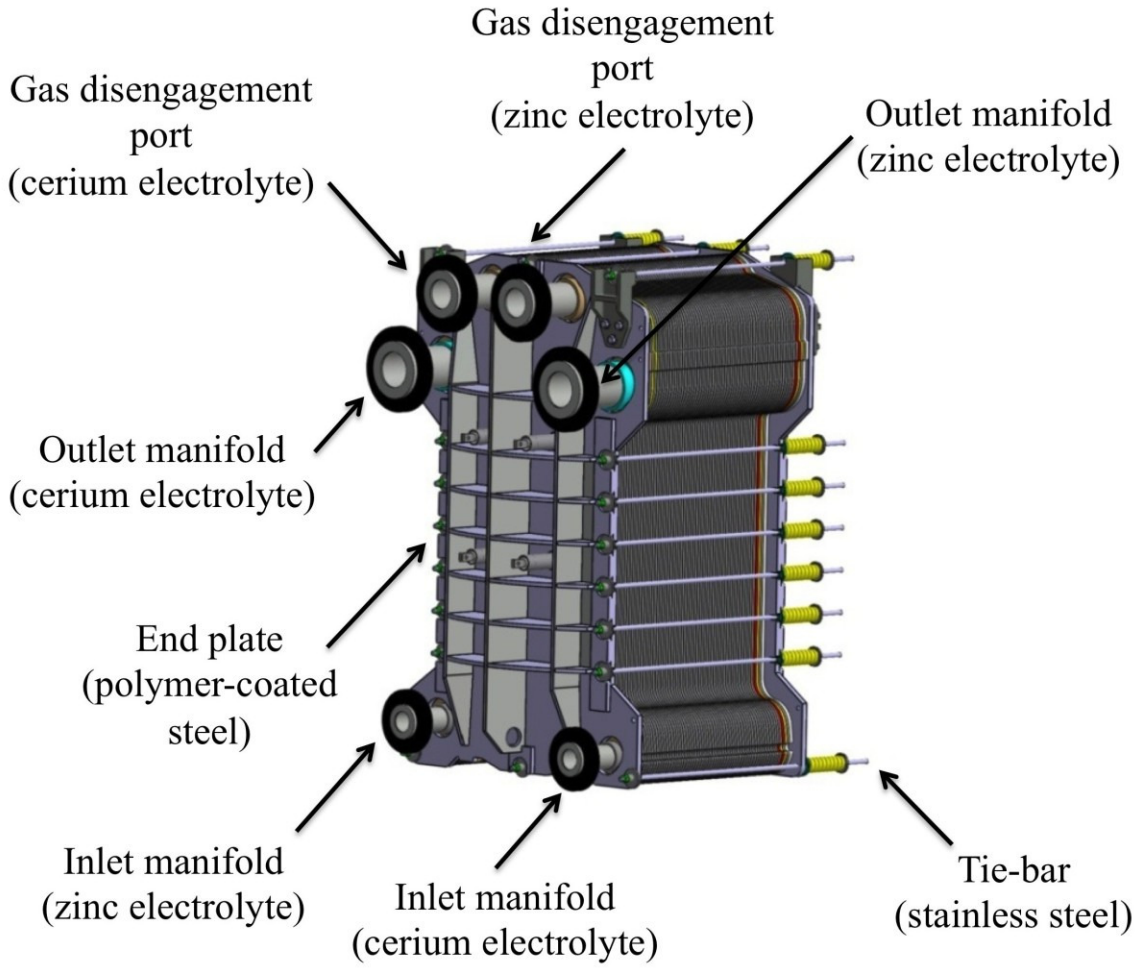
Gas disengagement port (cerium electrolyte)
Gas disengagement port (zinc electrolyte)
Outlet manifold (zinc electrolyte)
Outlet manifold (cerium electrolyte)
End plate (polymer-coated steel)
Inlet manifold (zinc electrolyte)
Inlet manifold (cerium electrolyte)
Tie-bar (stainless steel)

Figure 17a).

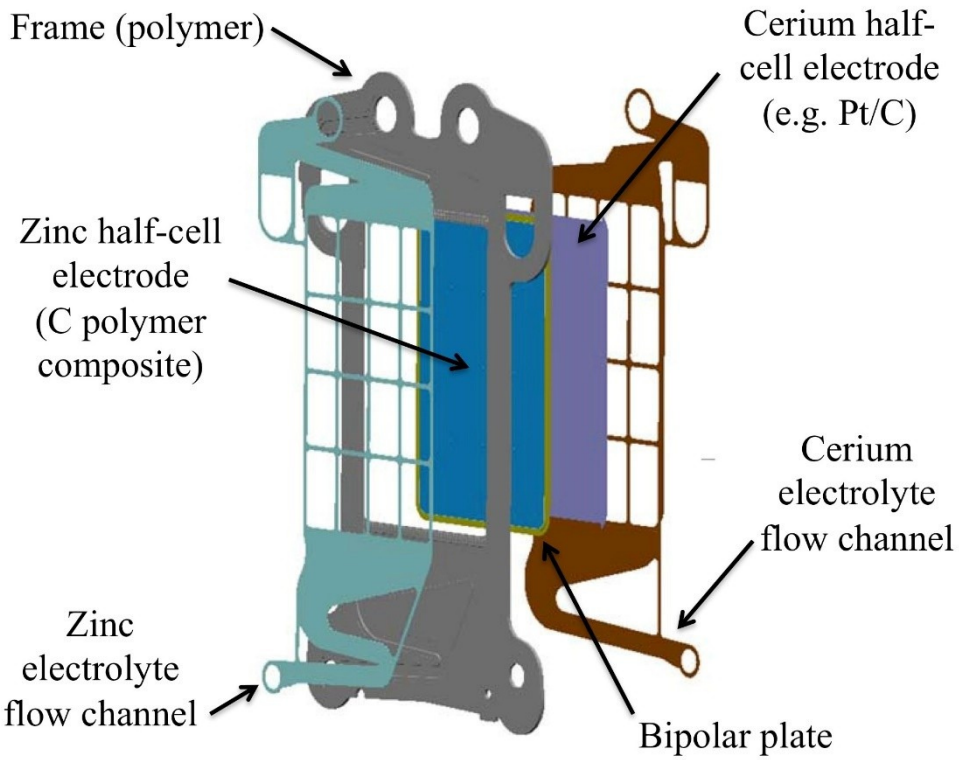
Frame (polymer)
Cerium half-cell electrode (e.g. Pt/C)
Zinc half-cell electrode (C polymer composite)
Cerium electrolyte flow channel
Zinc electrolyte flow channel
Bipolar plate

Figure 17b).

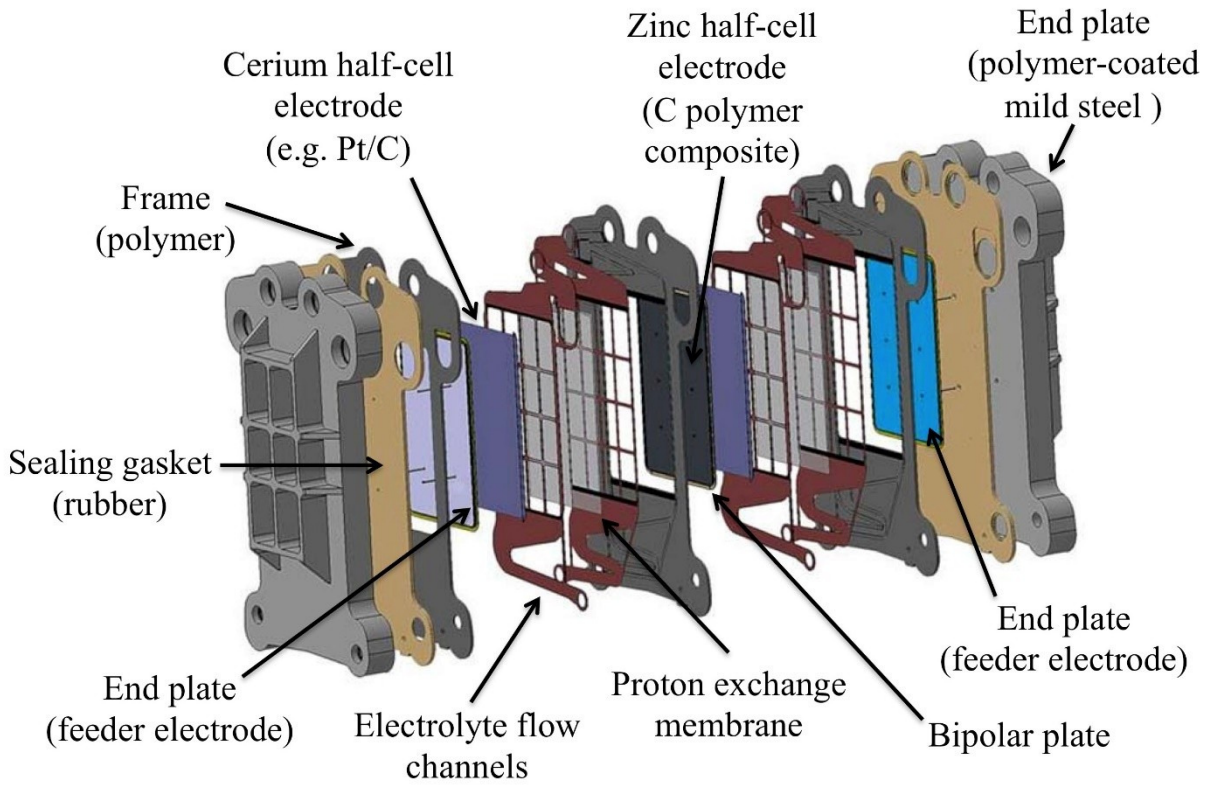
Cerium half-cell electrode (e.g. Pt/C)
Zinc half-cell electrode (C polymer composite)
End plate (polymer-coated mild steel)
Frame (polymer)
Sealing gasket (rubber)
End plate (feeder electrode)
End plate (feeder electrode)
Electrolyte flow channels
Proton exchange membrane
Bipolar plate

Figure 17c).

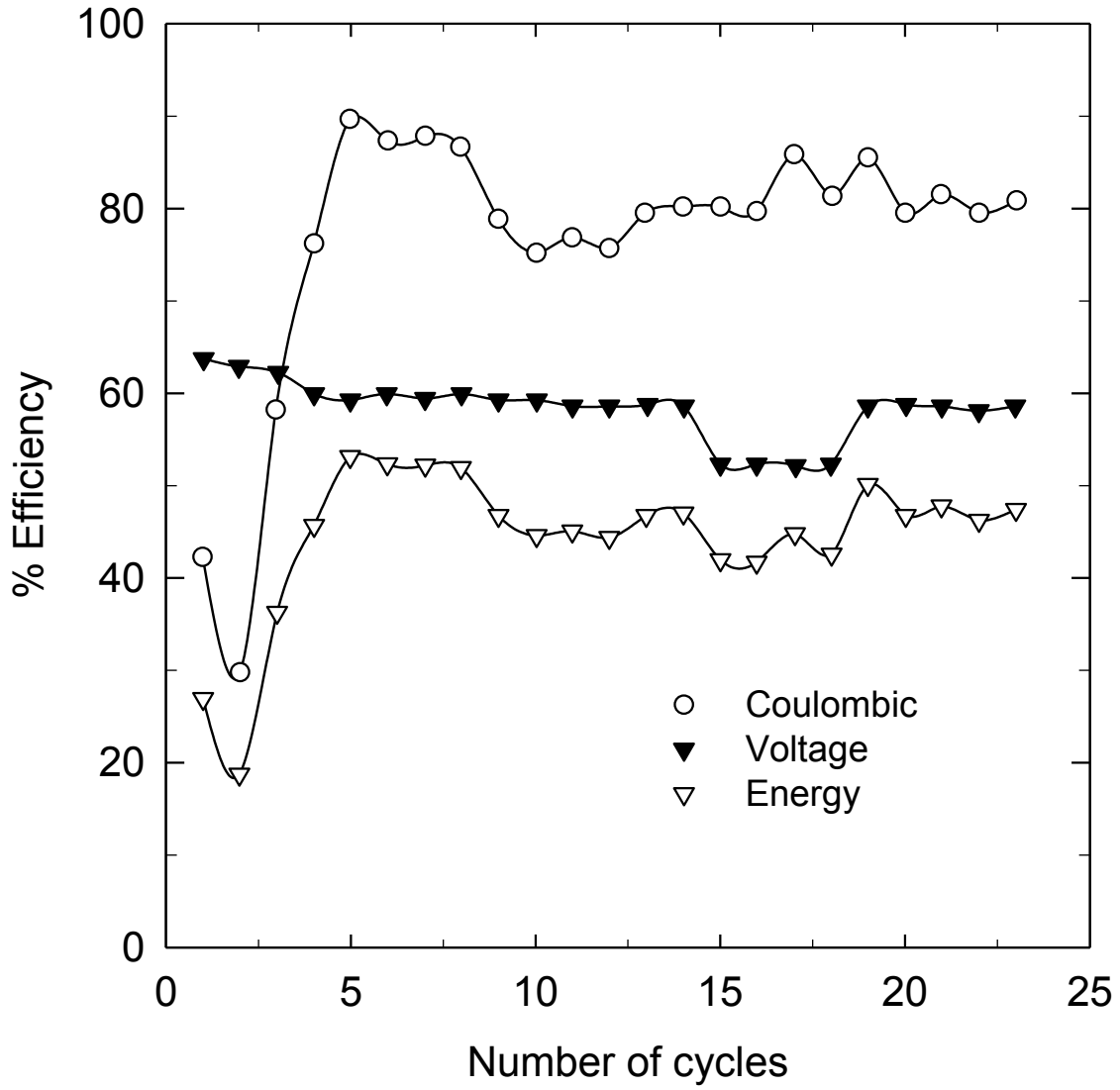
100
80
60
40
20
0
% Efficiency
0
5
10
15
20
25
Number of cycles
Coulombic
Voltage
Energy

Figure 18.